TURUN YLIOPISTON JULKAISUJA
ANNALES UNIVERSITATIS TURKUENSIS

SARJA - SER. A I OSA - TOM. 459

ASTRONOMICA - CHEMICA - PHYSICA - MATHEMATICA

MAGNETIC PROPERTIES OF CdSb DOPED WITH Ni AND ZnO CO-DOPED WITH Fe AND Mg

by

Ilari Ojala

TURUN YLIOPISTO
UNIVERSITY OF TURKU
Turku 2013

From the Wihuri Physical Laboratory
Department of Physics and Astronomy
University of Turku
Turku, Finland
and
National Graduate School in Materials Physics
Helsinki, Finland

Supervised by

Professor Reino Laiho
Wihuri Physical Laboratory
Department of Physics and Astronomy
University of Turku
Turku, Finland

Reviewed by

Prof. Sergey Ivanov
Ioffe Physico-Technical Institute
Polytekhnicheskaya 26
St. Petersburg, 194021
Russia

Assistant Prof. Petra Jönsson
Dept. of Physics and Astronomy
Uppsala University
Box 516
751 20 Uppsala
Sweden

Opponent

Dr. Vadim Sirkeli
Semiconductor Physics Laboratory
Moldova State University
60 A. Mateevici street
MD-2009 Chisinau
Moldova

ISBN 978-951-29-5327-1 (PRINT)
ISBN 978-951-29-5328-8 (PDF)
ISSN 0082-7002
Painosalama Oy - Turku, Finland 2013

Acknowledgements

This work has been carried out in Wihuri Physical Laboratory of the Department of Physics and Astronomy at University of Turku. I wish to thank National Graduate School in Materials Physics and Turku University Foundation for financial support.

I would like to express my sincere gratitude to Prof. Emer. R. Laiho for supervising and otherwise providing support for my thesis, and for arranging my graduate school position. I wish to thank Prof. P. Paturi and Dr. H. Huhtinen for all the help they have given me, and all my friends and colleagues at Wihuri Physical Laboratory for the inspirational atmosphere both during and outside the office hours. All my co-authors are also acknowledged.

I want to thank my parents for providing me the opportunity to follow the road that lead me to my scientific studies, and of course for all the support they have given me over the years. I'm also deeply indebted to my godmother Pirjo Suomi for kindling the spark of interest in physics in me.

Finally, I would like to dedicate this work to my wife Petra and son Carl. You mean the world to me.

Turku, February 2013

Ilari Ojala

Abstract

In this work, the magnetic properties of two different magnetic semiconductor materials, CdSb doped with 2 at.-% Ni and ZnO doped with Fe and Mg, were investigated. Samples of Ni-doped CdSb single crystals showed superparamagnetic behaviour, with the magnetic irreversibility decreasing with increasing external magnetic field, and the zero-field cooled (ZFC) magnetization displaying a broad maximum at a blocking temperature. Mean anisotropy field $B_K \sim 400$ mT and zero-field blocking temperature $T_b(0) \sim 100$ K values were obtained from the magnetic irreversibility measurements.

Magnetic properties of the Ni-doped CdSb samples were found to be anisotropic along the different crystallographic axes. The behaviour was explained by the presence of spheroidal Ni-rich $Ni_{1-x}Sb_x$ particles in the samples. Calculations and comparisons to the theory of superparamagnetism suggested that these particles had high aspect ratios and that they were broadly oriented around a preferred direction. Also, a broad particle size distribution could be inferred from the magnetization data.

Resistivity studies of the CdSb samples suggested a hopping-type conduction at low temperatures. Anisotropic hopping mechanisms were observed, along with a change in the mechanism between measurements at zero external field, and below weak field limit.

$Zn_{1-x}Fe_xO$ samples were found to exhibit paramagnetic behaviour at temperatures above 15 K. The measured magnetization of these samples was strictly proportional to the Fe content in the samples. Combination of the magnetization and structural data suggested that the magnetic properties of the samples were dominated by a secondary chemical phase, for which a likely candidate was found to be $ZnFe_2O_4$.

Co-doping the samples with Mg reduced the mass magnetization of the samples with low Fe doping level ($x = 0.01$). A deviation from the Curie–Weiss type paramagnetic behaviour at temperatures of 50–200 K was seen for Mg content of $y = 0.02$, and higher Mg doping levels changed the $M(T)$ curve shapes from concave to convex above 45 K. Single polarons and small clusters were suggested as the explanation for enhancement of the magnetization in the lowest temperatures.

Increase in the Fe content for samples with $y \geq 0.10$ increased the magnetization by two orders of magnitude compared to samples with $x = 0.01$. Curie temperatures (T_C) above 320 K were observed, and the high-temperature magnetization data was used for comparisons with simulations based on a thermally-activated RKKY model. Magnetization data above the T_C was also used for calculations based on critical behaviour of ferromagnets.

Preface

Articles included in this thesis

P1. R. Laiho, A. V. Lashkul, E. Lähderanta, K.G. Lisunov, I. Ojala, V. S. Zakhvalinskii: *Magnetic properties of CdSb doped with Ni*, Journal of Magnetism and Magnetic Materials **300**, e8 (2006).

P2. R. Laiho, A. V. Lashkul, K.G. Lisunov, E. Lähderanta, I. Ojala, V. S. Zakhvalinskii: *The influence of Ni-rich nanoclusters on the anisotropic magnetic properties of CdSb doped with Ni*, Semiconductor Science and Technology **21**, 228 (2006).

P3. E. Lähderanta, R. Laiho, A. V. Lashkul, K.G. Lisunov, I. Ojala, V. S. Zakhvalinskii: *Ni-rich nanoclusters in CdSb: influence on magnetic and transport properties and perspectives for spintronics*, Nanotechnology Perceptions **4**, 249 (2008).

P4. R. Laiho, I. Ojala, L. Vlasenko: *Percolation of ferromagnetism in ZnO codoped with Fe and Mg*, Journal of Applied Physics **108**, 053915 (2010).

Articles relevant to this work but not included in this thesis

P5. R. Laiho, A.V. Lashkul, K.G. Lisunov, E. Lähderanta, I. Ojala, V.S. Zakhvalinskii: *Ferromagnetic spheroidal Ni-rich nanoclusters in CdSb doped with Ni*, Moldavian Journal of the Physical Sciences, **Vol.7**, N1 (2008).

Contents

1 Introduction

1.1 Background

Spin-based electronics (spintronics) technology, where the electron spin instead of its charge is used to carry information, begun with the discovery of giant magnetoresistance (GMR) in 1988 [1]. First-generation spintronics devices are mainly based on GMR spin valve sensors; the most important application in the class being computer hard drives with their GMR read heads [2].

Second generation of spintronics applications are magnetoresistive random access memory (MRAM) devices. They store data using magnetic hysteresis and read it by a magnetoresistive method. One promising way for creating bits for MRAM is to use a magnetic tunnel junction storage cell [3]. The cell consists of two ferromagnetic layers separated by a non-magnetic tunneling barrier layer [4]. One ferromagnetic layer has its magnetization fixed in a certain direction, while the direction of the magnetization of the second layer (so-called free layer) can be changed with a local external field [5]. The orientation of the two layers' magnetizations with respect to each other sets the bit value of the cell, as shown in figure 1. The bit value is read by measuring the magnetoresistance of the cell. Write operation is done by manipulating the magnetization direction of the free layer.

The main advantage of MRAM compared to other solid-state memory types like static RAM (SRAM), dynamic RAM (DRAM) and Flash memory, is non-volatility combined with low read and write access times. Characteristic properties of these RAM technologies are presented in table 1. Overall, the combination of desirable characteristics in MRAM makes it a good candidate for ”universal” memory, which works as both random access memory and data storage, replacing currently-used RAM types (mainly DRAM) and storage devices like hard disk drives [6, 7]. Non-volatility is important for applications like instant-on computers, where the system state is stored in RAM when the computer is turned off and the state is restored when the power is turned on, without needing any separate process moving the data from the non-volatile storage to RAM [8]. Non-volatility also means that MRAM does not use any power in stand-by mode [9].

MRAM technology can also lead to further integration of digital circuits, for example by using logic-in-memory [10] architectures, where the memory modules are integrated onto same physical wafers as the logic processing units. These very large scale integrated circuits may achieve both short delays between the memory and the

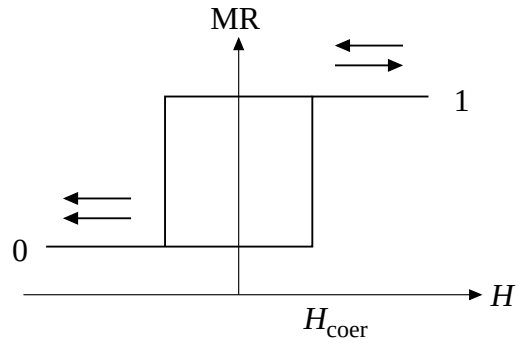

Figure 1. Magnetic hysteresis and bit values in an MRAM cell. MR is the measured magnetoresistance, H the external magnetic field, and H_{coer} the coercivity of the cell. The arrows indicate the magnetization directions of the cell's two magnetic layers.

Table 1. Comparison of MRAM's properties with other commonly used RAM technologies. [3]

Technology	SRAM	DRAM	MRAM	Flash
Read time	fast	moderate	moderate–fast	moderate
Write time	fast	moderate	moderate–fast	slow
Volatility	volatile	volatile	non-volatile	non-volatile
Minimum cell size	large	small	small	small
Write cycles	not limited	not limited	not limited	limited

processing unit and very low power usage [11]. Tight integration reduces the interpath complexity between the processor and the RAM, and offers naturally numerous data paths increasing the available communication bandwidth [9]; meanwhile non-volatility reduces power consumption as the registers do not require power for refreshing their contents.

Ease of integration with other electronic components is the main reason why materials based on semiconductors are suggested for making the second-generation spintronics devices [12]. Amongst different magnetic semiconductor types studied for spintronics materials, diluted magnetic semiconductors with their low magnetic dopant levels offer an option to use existing semiconductor manufacturing methods in device fabrication [13].

1.2 Diluted magnetic semiconductors

Diluted magnetic semiconductors (DMSs) combine a non-magnetic semiconductor with a transition metal (TM) dopant, *e.g.* Co, Cr, Cu, Fe, Ni, or Mn, resulting in interactions not present in the parent compounds. Among them are $s-d$ exchange interaction between band carriers and localized magnetic moments of the TM ions, and the $d-d$ interaction between the ions themselves. DMSs can be divided into two groups. In the first group are materials where the magnetic ions concentrate in nanosized regions inside the host semiconductor material, forming local condensed magnetic semiconductors (CMSs). Second group consists of materials that have the magnetic ions randomly distributed throughout the semiconductor matrix. [14]

Current research interests in these DMS compounds are mainly aimed towards second-generation spintronics applications, where high spin polarization of the charge carriers and compatibility with current semiconductor materials used in industry are desirable. For use in industrial scale, these materials should also have their magnetic Curie temperatures (T_C) above room temperature, and they should be available as both n- and p-type materials for direct use in semiconducting junction applications like transistors [15].

Most DMS materials studied so far have low T_C values, so they are not suitable for spintronics applications [2, 16]. These include Mn-doped III-V group semiconductors, which have been the most studied DMS materials [17]; for example T_C of only 110 K has been reported for $Ga_{1-x}Mn_xAs$ [18]. In 2000, room temperature ferromagnetism (RTFM) in Mn-doped p-type GaN and ZnO was predicted by Dietl *et al.* using Zener model [19]. These predictions were soon experimentally confirmed for both materials [20, 21]. Since then, RTFM has been reported in several other materials, like Co- or Cr-doped AlN [22] and Mn-doped GaP [23]. Especially dilute magnetic oxides like ZnO are a promising research field towards novel applications like transparent spintronics components [24].

1.2.1 Cadmium antimonide

Cadmium antimonide is a II-V group semiconductor with indirect energy gap 0.56 eV at 0 K [25]. At room temperature CdSb has orthorhombic structure with lattice parameters $a = 6.471$ Å, $b = 8.253$ Å, and $c = 8.526$ Å [26]. For the unit cell, see figure 2. The orthorhombic structure is linked to anisotropic electronic and magnetic properties of CdSb [25, 27]. Undoped CdSb shows diamagnetic behaviour [28].

Mixture of CdSb with about 2 mol % NiSb forms an eutectic system [29]. It has been

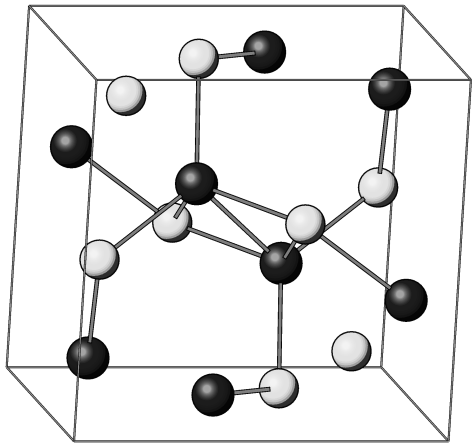

Figure 2. Unit cell of CdSb. Dark spheres represent Cd, light spheres Sb atoms.

observed that the NiSb particles grow inside the eutectic mixture with an orientation distribution around a preferred angle to the crystal growth direction. These needle-like particles have highly asymmetric shape, roughly 30–40 μm in length and with diameters of 1–1.5 μm [29]. Similar asymmetric microinclusions have been found in other Sb-based compounds, like InSb-TSb, where T = Fe, Ni, Mn, or Cr [30]. It can thus be expected that when the amount of Ni is below the eutectic level, smaller in physical dimensions, but still highly asymmetric Ni-rich particles are formed inside the CdSb matrix. The $Ni_{1-x}Sb_x$ phase is ferromagnetic up to $x \approx 0.075$ [31, p. 162]. In these samples, the overall magnetization consists of the diamagnetic contribution of the host CdSb lattice, and the ferromagnetic component of the embedded Ni-rich phase. At low enough Ni doping level, which determines the $Ni_{1-x}Sb_x$ particle size, the particles can be so small that superparamagnetic behaviour is possible.

1.2.2 Zinc oxide

Zinc oxide (ZnO) is a II-VI semiconductor with a wide direct band gap, about 3.4 eV at room temperature [32]. The crystal structure of ZnO, presented in figure 3, is hexagonal wurtzite with lattice parameters $a = 3.25$ Å and $c = 5.12$ Å [33].

The wide band gap means that ZnO is transparent to visible light, as 3.4 eV corresponds to a wavelength of about 360 nm, which is in the ultraviolet (UV) region. Therefore it is possible to use ZnO as a transparent conductor heavily doped *e.g.* with Al [34]. On the other hand, the wide gap makes ZnO attractive for blue and UV light

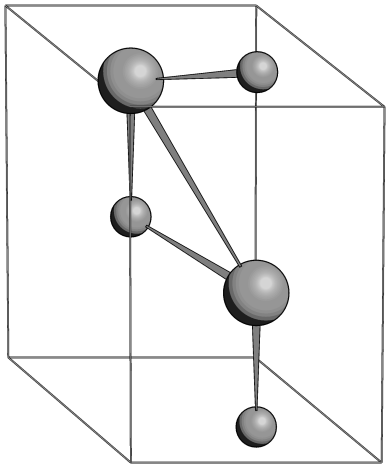

Figure 3. Unit cell of ZnO. Large spheres represent O and the smaller spheres Zn atoms.

optoelectronics, although the difficulty of p-type doping has been an obstacle for electronics use [35].

The initial work by Dietl *et al*. [19] sparked a wide interest in research of ZnO doped with transition metals, and the number of publications on ZnO-based DMOs increased from less than 10 in year 2000 to over 300 per year by 2007 [36]. Some examples of reported results are RTFM in Co- and Mn-doped bulk ZnO [37], and Curie temperatures up to 400 K in Cr- and Fe-doped ZnO films [38, 39]. Further theoretical predictions of Curie temperatures in ZnMeO compounds (Me = Mn, Fe, Co, Ni) were provided by Sandratskii and Bruno in 2006 [40]. Their calculated values of T_C in $Zn_{1-x}Fe_xO$ without co-doping of extra carriers were 453 K for $x = 0.25$, and 27 K for $x = 0.0625$.

In addition to TM-doped ZnO, RTFM has been reported in several other ZnO-based materials. These reports include Curie temperatures higher than 400 K due to Zn–C subsystem in C-doped ZnO films [41], and $T_C > 300$ K in $Zn_{1-x}B_xO$ films [42]. Ferromagnetism has been observed even in nanocrystalline powders [43] and thin films [44] of undoped ZnO. For undoped ZnO, *ab initio* calculations [45, 46] show that both oxygen interstitials and zinc vacancies in the ZnO lattice may lead to ferromagnetism in the material. Understanding the mechanisms of ferromagnetism in non-TM-doped ZnO is useful for the research of new ZnO-based DMS materials, as enhanced magnetic properties may be achieved by coupling the intrinsic and extrinsic magnetic properties.

1.3 Models of magnetism in magnetic semiconductors

1.3.1 Superparamagnetism

Consider a single-domain ferromagnetic nanosized particle with magnetic moment μ at temperature T. If the magnetic properties of the particle are uniaxially anisotropic, the anisotropy energy E_K is of the form [47]

$$E_K = KV \sin^2 \theta, \tag{1}$$

where K is the magnetic anisotropy energy density, V is the particle volume, and θ is the angle between the magnetic moment and the symmetry axis. There are two minima in the anisotropy energy, which are antiparallel magnetic moment orientations. In the Néel–Arrhenius model [48], thermal excitations switch the magnetic moment between the different directions with a frequency

$$f = f_0 e^{-\frac{KV}{k_B T}}, \tag{2}$$

where f_0 is a frequency factor of the order of 10^9 Hz [47] and k_B is the Boltzmann constant. Inverse of eq. (2) gives the mean time between two direction changes:

$$\tau = \tau_0 e^{\frac{KV}{k_B T}}, \tag{3}$$

where $\tau_0 = \frac{1}{f_0} \approx 1$ ns.

When the temperature is lowered so that $k_B T$ approaches the energy barrier KV from above, the thermal excitations do not have enough energy to overcome this barrier. This means a shift from rapid fluctuation of the magnetic moment direction to slow relaxation towards equilibrium. Blocking temperature, T_b, for superparamagnetic materials is defined so that the magnetic moment does not appreciably change during the measurement time, τ_{meas}. An expression for the blocking temperature can be derived from eq. (3) by setting $\tau = \tau_{meas}$ at $T = T_b$:

$$\tau_{meas} = \tau_0 e^{\frac{KV}{k_B T_b}}, \tag{4}$$

and thus

$$T_b = \frac{KV}{\ln \frac{\tau_{meas}}{\tau_0}}. \tag{5}$$

Using a typical $\tau_{meas} \sim 10^2$ s for a SQUID magnetometer, the equation becomes

$$T_b \approx \frac{KV}{25 k_B}. \tag{6}$$

So, for superparamagnetic particles, there exists a blocking temperature T_b, above which one can observe superparamagnetic behaviour driven by thermal excitations. Below T_b spontaneous magnetization and magnetic hysteresis is observed. In macroscopic measurements one can observe the effects of blocking as an irreversibility between zero-field cooled (ZFC) and field cooled (FC) magnetization curves. In addition, there is a maximum in ZFC magnetization at low temperatures.

An external magnetic field reduces the anisotropy energy barriers and decreases the blocking temperature T_b. The dependence of T_b on the external magnetic field B is given [49] by an approximate relation

$$\left[\frac{T_b(B)}{T_b(0)}\right]^{\frac{1}{2}} = 1 - \frac{B}{B_\mathrm{K}}, \tag{7}$$

where B_K is the mean anisotropy field. At $B \sim B_\mathrm{K}$ the magnetic irreversibility vanishes. It has also been found [49] that

$$\frac{B_\mathrm{K}}{T_b(0)} \approx \frac{2k_\mathrm{B}}{\mu} \ln \frac{\tau_{meas}}{\tau_0}. \tag{8}$$

For the typical measurement time $\tau_{meas} \sim 10^2$ s,

$$\frac{B_\mathrm{K}}{T_b(0)} \approx 50 \frac{k_\mathrm{B}}{\mu}. \tag{9}$$

There are three main restrictions for the validity of the equations (2)–(9) [50]:

1. The particle assembly should consist only of single-domain particles. The upper size limit for single-domain particles is given by the critical radius r_{sd} defined by the equation [50]
$$\frac{N_c (M_s^*)^2 r_{sd}^2}{6A} = \ln \frac{4r_{sd}}{a} - 1, \tag{10}$$
where N_c is the demagnetization factor for fields parallel with the major axis of a spheroidal particle (values for minor and major axes can be found for example in [51]), M_s^* is the saturation magnetization at 0 K, a is the mean distance between the magnetic ions, and A is exchange stiffness constant of the cluster material.

2. In magnetization reversal the spins rotate in unison keeping a parallel orientation, *i.e.* the reversal process is a coherent rotation [52, pp. 389–390]. The critical radius for occurrence of the coherent rotation is [50, 53]
$$r_c = \frac{q}{M_s^*} \sqrt{\frac{2A}{N_a}}, \tag{11}$$

where $N_a(m)$ is the demagnetization factor for the minor axis, m is the aspect ratio of the particle, and q is the related smallest solution for the Bessel functions J_1 of the first kind (limiting values are $q = 1.8412$ for an infinitely long cylinder with $m \to \infty$; and $q = 2.0816$ for a sphere with $m = 1$).

3. The interaction energy W between the clusters is small compared to the anisotropy energy.

For particles with radius r, the requirements 1–3 above can be summarized by $r \ll r_{sd}$, $r \ll r_c$, and $W \ll KV$, respectively.

In a more general case, the temperature dependence of coercivity field B_c for blocked nanoparticles is given [54] by

$$B_c^{(j)}(T) = B_c^{(j)}(0)\left[1 - \left(\frac{T}{T_b(0)}\right)^n\right], \tag{12}$$

where j notes the crystallographic axis, $j = 1$, 2, and 3, and $B_c^{(j)}(0)$ and n depend on the magnetization reversal mode. Comparison with eq. (7) shows that $n = \frac{1}{2}$ for coherent rotation. In the case of coherent rotation of randomly oriented spheroidal particles, $B_c^{(j)}(0)$ is given [55, p. 831] by the equation

$$B_c^{(j)}(0) = \alpha^{(j)} B_{\mathrm{K}}, \tag{13}$$

where $\alpha^{(j)} = 0.479$ for any j. For non-random orientations with preferred direction

$$\alpha^{(j)} = \begin{cases} (\cos^{2/3}\theta_j + \sin^{2/3}\theta_j)^{-3/2} & \text{if } 0 < \theta_j < 45^\circ \\ \sin\theta_j \cos\theta_j & \text{if } 45^\circ < \theta_j < 90^\circ, \end{cases} \tag{14}$$

where θ_j is the angle between the jth crystallographic axis and the major axis of the spheroid [51]. Angles θ_j satisfy the relation

$$\cos^2\theta_1 + \cos^2\theta_2 + \cos^2\theta_3 = 1. \tag{15}$$

Increasing the particle size so that $r_c \ll r \ll r_{sd}$ leads to magnetization reversal by curling [50], where $n = \frac{2}{3}$ [54]. In this reversal mode, the separate spins are turning in unison along the anisotropy axis, but they are also twisted radially in the plane perpendicular to the anisotropy axis, preserving cylindrical symmetry [52, pp. 393–394]. The difference between coherent rotation and curling is shown schematically in figure 4. In this regime the coercivity is [53]

$$B_c^{(j)}(0) = 2\pi M_s^* \frac{\left(2D_c - \frac{\kappa}{S^2}\right)\left(2D_a - \frac{\kappa}{S^2}\right)}{\sqrt{\left(2D_c - \frac{\kappa}{S^2}\right)^2 \sin^2\vartheta_j + \left(2D_a - \frac{\kappa}{S^2}\right)^2 \cos\vartheta_j}}, \tag{16}$$

where $D_a \equiv \frac{N_a(m)}{4\pi}$, $D_c \equiv \frac{N_c(m)}{4\pi}$, $S = \frac{r}{r_0}$, $r_0 = \frac{A^{\frac{1}{2}}}{M_s^*}$, $\kappa = \frac{q^2}{\pi}$, and ϑ is the angle between the major axis and an external magnetic field. If the sample contains particles with non-homogenous size and orientation distributions, the values of θ_j, r, and m can be approximated by their mean values. For a high enough aspect ratio, this approximation means that the magnetization directions of the spheroids are close to their major axis direction, and the components of the saturation magnetization at 0 K are given by

$$M_s^{(j)}(0) = \eta M_s^* [1 - D(\theta_j)] \cos\theta_j, \tag{17}$$

where η is the volume fraction of the magnetic phase in the sample, and

$$D(\theta_j) = D_a \sin^2\theta_j + D_c \cos^2\theta_j, \tag{18}$$

which is constrained by

$$D(\theta_1) + D(\theta_2) + D(\theta_3) = 1. \tag{19}$$

In a more general case, the mean magnetization direction is not parallel to the major axis of the particle. We assign φ_j for the components of the angle between the jth component of the direction of the magnetization and the corresponding component of the major axis, and find that

$$\tan\varphi_j = \frac{\left(\frac{X}{Y}\right)^{\frac{1}{2}} \tan\theta_j}{\left(\frac{X}{Y}\right)^{\frac{1}{2}} + \tan^2\theta_j}, \tag{20}$$

where $X = \left(2D_c - \frac{\kappa}{S^2}\right)^2$ and $Y = \left(2D_a - \frac{\kappa}{S^2}\right)^2$. Finally, we eliminate M_s^* using equations (16) and (17), which leads to

$$\cos\theta_j = \frac{2X + Y - Z_j X}{Z_j (Y - X)}, \tag{21}$$

where

$$Z_j = \left[B_c^{(j)}(0)\right]^2 \sum_{j=1}^{3} \left[B_c^{(j)}(0)\right]^{-2}. \tag{22}$$

Increasing the radius of the particles to $r > r_{sd}$ leads to magnetization reversal by weakly pinned domain walls, with $n = 1$ [56]. In a sample with a large particle size distribution, all the above regimes may be present, leading to a more complex macroscopical behaviour. Based on the broad separation of DMS materials into two groups as presented in section 1.2, it is clear that superparamagnetism is a likely model for CMS-type materials.

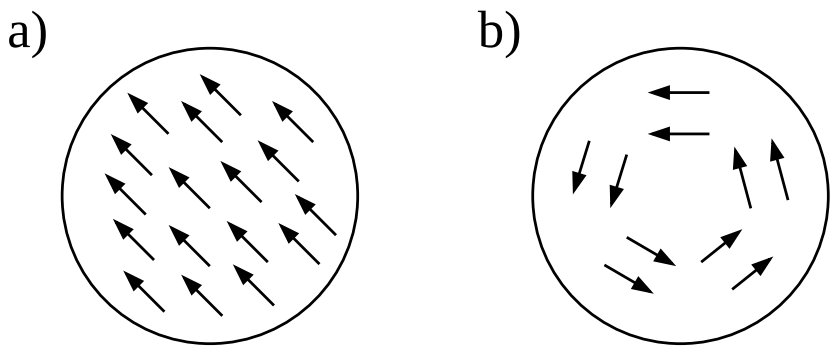

Figure 4. Magnetization reversal modes presented for cross-section of a long cylinder in magnetic field parallel to the major axis of the cylinder: a) coherent rotation, b) curling. The arrows indicate the spin directions. [52, p. 392]

1.3.2 Ruderman-Kittel-Kasuya-Yosida and Zener interaction

Zener suggested [57] in 1951 an interaction between the conduction electrons and unfilled inner shell electrons as a mechanism for ferromagnetism in metals with incomplete d-shells. This phenomenological Zener or $s-d$ interaction model was the basis for further studies to find similar mechanisms that could also account for antiferromagnetism and spin wave modes [58].

Ruderman and Kittel showed in 1954 how localized spins in a metal can couple through polarization and propagation of conduction electrons [59]. The wave function of a conduction electron is distorted near a localized spin by mixing with other wave functions of electrons with the same spin direction. For electron spins that are parallel to the localized spin, the distortion creates a maximum at the localized spin site, and it is shown [60] that only states above Fermi level contribute to the summed up wave function. The result is a sum over a range of wave vectors (corresponding to different wavelengths) which are in phase at the site of the localized spin. As the distance from the localized spin position increases, the different wave vectors get out of phase and create a damped oscillating distribution of electron spin density around the localized spin. Electron spins that are antiparallel to the localized spin behave similarly, with the localized spin site now being the position of the minimum for the wave functions.

The electron wave function seen by a second localized spin in the vicinity of the first one depends on the orientation and the distance between the two localized spins, and the resulting indirect coupling between the localized spins at relatively large distances D varies as $D^{-3}\cos(2k_{\mathrm{F}}D)$ [59], where k_{F} is the Fermi wave vector. The sign of the coupling constant determines the coupling type: positive values lead to ferromagnetic-type coupling, while negative sign means antiferromagnetic coupling. The distance dependence of coupling constant is plotted in figure 5. This indirect interaction is called Ruderman-Kittel-Kasuya-Yosida or RKKY interaction. [58, 59, 61]

Calderón and Das Sarma suggested in 2007 an RKKY-type mechanism where the exchange interaction is mediated by thermally excited carriers [62]. In this model, the density of carriers, n_c, is given by

$$n_c(T,\Delta) = n_{c0}e^{-\frac{\Delta}{k_{\mathrm{B}}T}}, \tag{23}$$

where Δ is the activation energy for the carriers, and n_{c0} is the density of trapped carriers. In an intrinsic semiconductor with magnetic impurities the Hamiltonian $\mathscr{H}$ of the exchange interaction between the impurity spins $\mathbf{S}_i$ and the carrier spin density $\mathbf{s}(\mathbf{r})$ is

$$\mathscr{H} = \sum_i J_{\mathrm{m}} a_0^3 \mathbf{S}_i \cdot \mathbf{s}(\mathbf{R}_i), \tag{24}$$

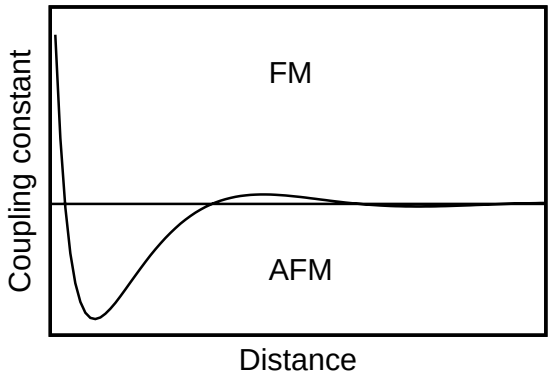

Figure 5. The dependence of the coupling constant on distance in RKKY model. The interaction type is alternating between ferromagnetic (FM) and antiferromagnetic (AFM) coupling.

where J_{m} is the local coupling between the impurity spin located at $\mathbf{R}_i$ and the carrier spin density, a_0^3 is the unit cell volume, and the sum is taken over all magnetic ions. Using a mean-field approximation in the limit of nondegenerate carriers results in a situation where the carrier spins see the impurity spins as an effective magnetic field proportional to $J_{\mathrm{m}} a_0^3 n_i \langle S_z \rangle$ [63]. Here n_i is the impurity density and $\langle S_z \rangle$ is the impurity spin expectation value [64]

$$\frac{\langle S_z \rangle}{S} = \mathscr{B}_S \left(\frac{H_{\mathrm{eff}}^i}{k_{\mathrm{B}} T} \right), \tag{25}$$

where H_{eff}^i is the effective field for the impurity spin site, and $\mathscr{B}_S$ is the Brillouin function:

$$\mathscr{B}_J(x) = \frac{2J+1}{2J} \coth\left(\frac{2J+1}{2J} x \right) - \frac{1}{2J} \coth\left(\frac{1}{2J} x \right). \tag{26}$$

For electrons on partly filled 3*d*-shells, the total angular momentum J can be replaced by the spin term. This is because such electrons are not screened in transition metals, and the spin-orbit coupling breaks down. [65, p. 30]

Symmetrically, the impurity spins are acted on by an effective field of the carrier spins, which is proportional to $J_{\mathrm{m}} a_0^3 n_c \langle s_z \rangle$, and the expectation value for the carriers spins is written as

$$\frac{\langle s_z \rangle}{s} = \mathscr{B}_s \left(\frac{H_{\mathrm{eff}}^c}{k_{\mathrm{B}} T} \right), \tag{27}$$

where H_{eff}^c is the effective field for the carriers. As the effective fields H_{eff}^i and H_{eff}^c are already given by the mean-field approximation, eqs. (25)–(27) lead to a self-consistent

expression for the magnetization of the impurity spins:

$$\frac{\langle S_z \rangle}{S} = \mathscr{B}_S \left[\frac{J_m a_0^3 n_c(T,\Delta)}{k_B T} s \mathscr{B}_s \left(\frac{J_m a_0^3 n_i \langle S_z \rangle}{k_B T} \right) \right]. \tag{28}$$

1.3.3 Bound magnetic polarons

A bound magnetic polaron is formed when charge carriers with non-uniform spin polarization are localized near a donor or acceptor impurity. Coulomb attraction between the impurity and the charge carriers is the main mechanism for the localization [66]. The polaron radius R_p at temperature T is given [67] by the equation

$$R_p(T) = \frac{a_B}{2} \ln \frac{sS|J| \left(\frac{a_0}{a_B}\right)^3}{k_B T}, \tag{29}$$

where a_B is the Bohr radius, a_0^3 is the unit cell volume, s is the carrier spin, S is the spin of the magnetic impurity, and J is the exchange parameter between the impurity and the carrier spins.

Bound magnetic polarons can lead to long-range ferromagnetic order, if the polaron density and size in the material are high enough for the polarons to overlap [16]. Starting at a temperature much above T_C, there are no polarons. The polarons start to appear at $k_B T \sim sS|J| \left(\frac{a_0}{a_B}\right)^3$ [67], then the polaron radii grow with lowering temperature, and finally overlapping polarons fill the whole material at T_C [68].

Oxygen vacancies can act as donors in DMO materials [16]. Figure 6 schematically presents polarons in an $A_{1-x}T_xO$ type material with oxygen vacancies, where A is a non-magnetic cation, and T is a transition metal dopant. Study of native point defects shows that oxygen and zinc vacancies are the most abundant defects in ZnO [69]. Zn interstitials have also been reported [70] to lead to shallow donor states in this material.

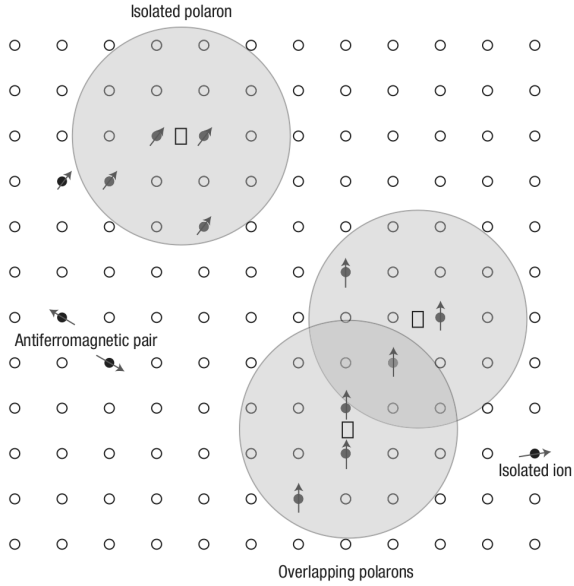

Figure 6. Bound magnetic polarons in an $A_{1-x}T_xO$ type material with oxygen vacancies. Oxygen sites are not presented, except the oxygen vacancies, which are marked with rectangles. Open circles represent A ions, black circles the T ions with the arrows indicating their spin directions, and the gray circles mark the polaron radii. [16]

1.3.4 Itinerant electrons and Stoner model of ferromagnetism

W. Pauli first showed in 1927 [71] that a gas of non-interacting itinerant electrons combined with the collective electron band model in crystals [72, pp. 28–37] leads to weak paramagnetism, *i.e.* Pauli paramagnetism. Susceptibility χ_P of this electron gas is proportional to the density of the states $N(\varepsilon_\mathrm{F})$ at Fermi energy,

$$\chi_\mathrm{P} = 2\mu_\mathrm{B}^2 N(\varepsilon_\mathrm{F}), \tag{30}$$

where μ_B is the Bohr magneton

$$\mu_\mathrm{B} = \frac{e\hbar}{2m_\mathrm{e}}, \tag{31}$$

where e is elementary charge, $\hbar$ is reduced Planck constant, and m_e is electron rest mass.

Stoner model of ferromagnetism considers itinerant electrons with repulsive interactions. The interactions are taken into account by adding a Weiss molecular field [73, pp. 100–104] type term. The equilibrium Fermi energy level, ε_F, is split and shifted by the molecular field (and an external field) experienced by the electrons to new values ε_F^+ and ε_F^- for spin-up and spin-down electrons, respectively. This new situation with separate Fermi levels is equivalent to the electrons of different spins sharing the same Fermi level, but the band is shifted by ΔE for those electrons having negative spins. Figure 7 shows a simplified illustration of the spin-splitting caused by the molecular field.

In this model, ΔE is directly proportional to the difference in the number of spin-up and spin-down electrons, n^+ and n^-, respectively:

$$\Delta E = I(n^+ - n^-)\mu_\mathrm{B}, \tag{32}$$

where I is called the Stoner exchange factor. Susceptibility χ_S at 0 K is

$$\chi_\mathrm{S} = \frac{2\mu_\mathrm{B}^2 N(\varepsilon_\mathrm{F})}{1 - IN(\varepsilon_\mathrm{F})} = \frac{\chi_\mathrm{P}}{1 - IN(\varepsilon_\mathrm{F})}, \tag{33}$$

so Pauli paramagnetism is enhanced by a factor of $1 - IN(\varepsilon_\mathrm{F})$ in the Stoner model. For $IN(\varepsilon_\mathrm{F}) \geq 1$ (so-called Stoner criterion), the system exhibits spontaneous magnetic order. [74, pp. 342-343]

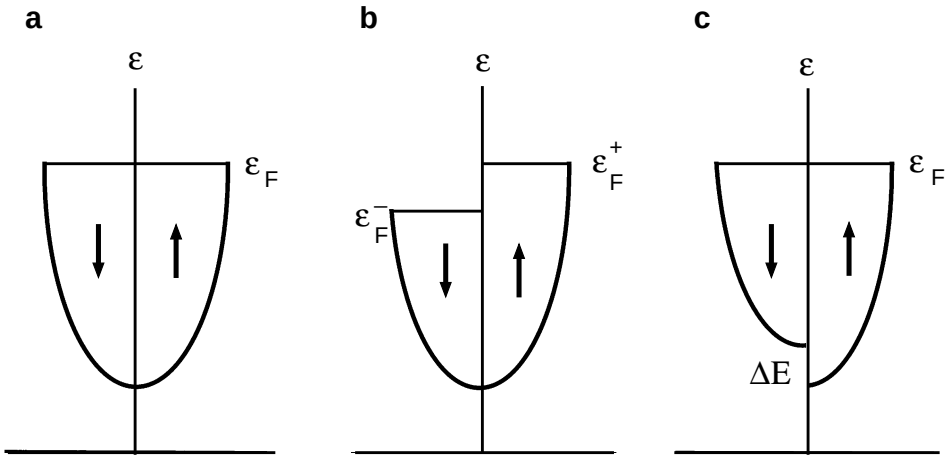

Figure 7. Stoner model of ferromagnetism. a) Equilibrium state with no molecular field. b) Molecular field shifts the Fermi levels. c) ε_f^+ and ε_f^- replaced for common ε_f, showing a spin splitting energy ΔE.

1.4 Hopping conductivity and magnetoresistivity

N. F. Mott studied in 1969 [75] a model of conductivity in insulators where the charge carriers are hopping with a thermally excited process between randomly based potential wells. He found that temperature dependence of the conductivity has the form

$$\sigma(T) \propto e^{-\left(\frac{T_{0\mathrm{M}}}{T}\right)^{1/(d+1)}}, \tag{34}$$

where d is the dimensionality of the system and $T_{0\mathrm{M}}$ is a constant depending on dimensionality, localization length, and the density of states at the Fermi level. The expression for 3D case,

$$\sigma(T) \propto e^{-\left(\frac{T_{0\mathrm{M}}}{T}\right)^{1/4}}, \tag{35}$$

and the model is called Mott variable-range hopping (VRH) conductivity, where [76]

$$T_{0\mathrm{M}} = \frac{\beta_{\mathrm{M}}}{k_{\mathrm{B}} N(\varepsilon_{\mathrm{F}}) a^3} \tag{36}$$

with $\beta_{\mathrm{M}} = 21$ [77, p. 206] and a is localization radius of the charge carriers.

In Mott VRH conductivity, constant (and finite) density of states at Fermi level is assumed. However, Pollak [78] followed by Ambegaokar *et al.* [79] soon questioned the validity of this assumption in the general case. As the density of the states should be reduced by electron-electron Coulomb interaction, Mott VRH model works only in the cases where long-range Coulomb interaction is screened. In 1975 Efros and Shklovskii introduced a model which takes the Coulomb interaction into account [80]. Temperature-dependent Shklovskii–Efros (SE) type VRH conductivity is [77, p. 240]

$$\sigma(T) \propto e^{-\left(\frac{T_{0\mathrm{SE}}}{T}\right)^{1/2}}, \tag{37}$$

where

$$T_{0\mathrm{SE}} = \frac{\beta_{\mathrm{SE}} e^2}{\varepsilon_r k_{\mathrm{B}} a}, \tag{38}$$

$\beta_{\mathrm{SE}} = 2.8$ [77, p. 344], and ε_r is the dielectric constant. Contrary to Mott VRH, $\sigma(T)$ does not depend on the dimensionality of the system in SE VRH.

At higher temperatures, the hopping probability is limited by proximity of the potential wells [81, p. 1043]. This is the nearest-neighbour hopping (NNH) regime, where the conductivity is given [82] by

$$-\ln\sigma \propto T^{-1}. \tag{39}$$

In a more general case, we can write for the resistivity $\rho(T) = \frac{1}{\sigma(T)}$ a universal equation:

$$\rho(T) = DT^m \exp\left[\left(\frac{T_0}{T}\right)^p\right], \tag{40}$$

where D is a constant, T_0 is a characteristic temperature and $m = p$ for hydrogenic wave functions of the localized electron [27]. Comparing eq. (40) to the previous eqs. (35), (37), and (39) for different hopping conductivity types, $p = 1$ for NNH, $p = \frac{1}{2}$ and $T_0 = T_{0\mathrm{SE}}$ for SE VRH, and $p = \frac{1}{4}$ with $T_0 = T_{0\mathrm{M}}$ for 3D Mott VRH.

The dependence of magnetoresistance $\frac{\rho(B)}{\rho(0)}$ (MR) on external field for hopping conductivity in weak fields is predicted [77, pp. 163–165] to be

$$\ln\frac{\rho(B)}{\rho(0)} \propto B^2. \tag{41}$$

The upper limit for the regime of weak fields is given by a characteristic critical field B_{crit} [83].

In general, there is a small positive component of MR, which is connected to shrinking impurity wave functions in the direction perpendicular to the external field [77]. However, the temperature dependence of MR is determined by the hopping type. Concerning NNH in a weakly doped semiconductor with magnetic anisotropy, MR is given [84] by the equation

$$\ln\left[\frac{\rho(B)}{\rho(0)}\right]_j = C_j B^2, \tag{42}$$

where

$$C_j = \frac{te^2 a p_j^2}{\hbar^2 N_a}, \tag{43}$$

where $t = 0.036$, N_a is impurity concentration, p_j is anisotropy coefficient [27], and index $j = 1, 2, 3$ refers to magnetic field direction perpendicular to the electric current direction. Notably C_j does not depend on temperature.

For Mott VRH and SE VRH cases, MR depends on temperature. The equations for VRH in an anisotropic semiconductor in weak field B are [84]

$$\ln\left[\frac{\rho(B)}{\rho(0)}\right]_j = \frac{t_1 e^2 a^4 p_j^2}{\hbar^2}\left(\frac{T_{0M}}{T}\right)^{\frac{3}{4}} B^2 \equiv A_{0j}^{(M)} T^{-\frac{3}{4}} B^2 \tag{44}$$

with $t_1 = \frac{5}{2016}$ [77, p. 211] for Mott VRH, and

$$\ln\left[\frac{\rho(B)}{\rho(0)}\right]_j = \frac{t_2 e^2 a^4 p_j^2}{\hbar^2}\left(\frac{T_{0SE}}{T}\right)^{\frac{3}{2}} B^2 \tag{45}$$

with $t_2 = 0.0015$ [77, p. 213] for SE VRH.

2 Experimental

2.1 Sample preparation

CdSb single crystal samples doped with 2 atomic percent of Ni were prepared by a two-stage modified Bridgman method [25]. First, Ni was dissolved in Cd at 700 °C. Stoichiometric amounts of the Cd-Ni mixture and Sb were then deposited into a quartz ampoule, which was heated to 460 °C, and after 12 h slowly cooled down to room temperature. X-ray diffraction methods were used to determine the crystalline orientation of the grown ingots, and rectangular prisms sized about $6 \times 2 \times 2$ mm^3 were cut from the ingots so that one of the [100], [010], and [001] crystallographic axes would align with the long side of the prism.

ZnO-based samples were prepared via two routes:

(i) In the solid-state reaction method stoichiometric amounts of ZnO and oxides of the dopants (Fe_2O_3 or MgO) were ground in powder form, then calcinated at 500 °C to form a precursor powder.

(ii) Citrate-gel method [85] started with water solutions of high-purity nitrate salts of Zn, Fe, and Mg. The solutions were mixed in stoichiometric proportions for the wanted sample formula, then citric acid and ethyldiamine were added to the mixture, until pH of the solution reached 5.2. Water was evaporated from the solution at 80 °C, and the resulting gel was fired at 500 or 1000 °C to obtain the precursor powder. Ceramic pellets were made by pressing the precursor powder and sintering the pellet at 700 °C.

2.2 X-ray diffraction

Crystallographic studies of the ZnO powders and pellets were made with *Philips XPert Pro* x-ray diffraction (XRD) system in $\theta - 2\theta$ geometry. Illustration of x-ray diffraction is presented in figure 8. Constructive interference of the incoming x-rays is observed at point P, if the difference of the distances which the rays have travelled is a multiple of the wavelength λ. This leads to Bragg's law

$$2d_{hkl} \sin\theta = \lambda, \tag{46}$$

where (hkl) is the reflecting plane written with Miller's indices, d_{hkl} is the distance between the planes, and θ is the angle between the incoming x-ray and the reflecting crystal plane.

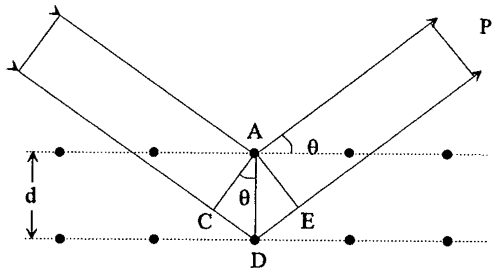

Figure 8. Diffraction of the x-rays from the atom layers in the sample.

Chemical compounds present in the sample can be determined in $\theta - 2\theta$ x-ray diffraction measurement, where the wavelength of the x-rays coming from the x-ray tube and the incident angle θ are known. X-ray diffractogram (reflected intensity as a function of the diffraction angle 2θ) is recorded for the sample. As the measured diffractogram is a superposition of the diffractograms of all the elements and compounds in the sample, comparison with literature data can be used to deduce the chemical composition of the sample. In powder diffraction measurements the peak intensity in the diffractogram is proportional to the abundance of different elements sample and so these measurements give information about the chemical composition of the sample. A schematic presentation of a $\theta - 2\theta$ measurement setup is shown in figure 9.

Powder diffraction experiments were used to estimate the average particle size in the samples. Full width at half maximum (FWHM) value is measured from a chosen diffraction peak observed at an angle 2θ in the diffractogram, and the average particle diameter D is calculated from the Scherrer formula

$$D = 0.9\frac{\lambda_{CuK_\alpha}}{\Delta\cos(2\theta)}, \tag{47}$$

where λ_{CuK_α} is the Cu K_α radiation wavelength (0.15418 nm) used in the measurement, and Δ is the normalized peak FWHM value calculated from equation

$$\Delta = \sqrt{\sigma^2 - \sigma_I^2}, \tag{48}$$

σ is the measured peak FWHM, and σ_I is the FWHM measured from the peak of a reference sample. In this work pure Al_2O_3 sample was used as the reference.

2.3 Atomic force microscopy

Atomic force microscopy (AFM) studies of the ceramic ZnO sample surfaces were made with *Park Scientific Instruments Autoprobe CP-Research system*. The measure-

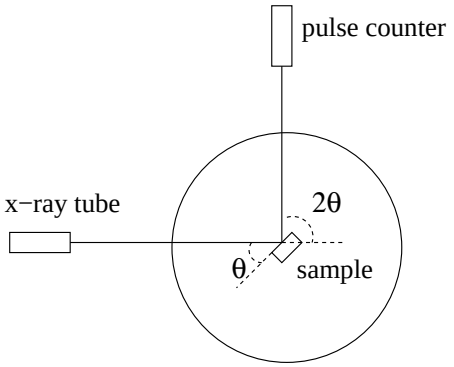

Figure 9. Schematic of the x-ray diffraction experiment in $\theta - 2\theta$ geometry.

ments were made in the contact mode, using image sizes of $3 \times 3 - 50 \times 50$ μm^2. In this mode, a small mechanical tip attached on a cantilever is scanned over the sample surface. In the measurement, the Van der Waals force existing between the tip and the features of the sample surface causes changes in the cantilever position, and these changes are detected with a laser beam that is reflected from the top of the cantilever to a position-sensitive photodetector. The height profile of the sample surface is then reconstructed from the recorded map of the deflections of the cantilever.

2.4 Magnetometer measurements

A radio frequency superconducting quantum interference device (RF SQUID) magnetometer was used for magnetic measurements of the samples. An RF SQUID consists of a flux transformer, a SQUID probe, and a resonant tank circuit. The flux transformer is a pickup loop connected directly to an input coil of the SQUID. The single Josephson junction SQUID is inductively connected to a tank circuit driven by an RF frequency current I_{RF}. When a magnetized sample travels through the flux pickup loop of the magnetometer, it causes a change in the magnetic flux running through the SQUID loop, which is detected by a change in the RF voltage V_{RF} across the SQUID tank circuit. The resulting voltage oscillation has a period of one flux quantum ($\Phi_0 = h/2e$), so the magnetization M of the sample can be calculated knowing that the total flux Φ through the SQUID loop is

$$\Phi = \int (B_0 + \mu_0 M) \mathrm{d}S, \tag{49}$$

where B_0 is an applied magnetic field density, dS is the element of the surface restricted by the loop and μ_0 is vacuum permeability. As the external field B_0 is known, M can be

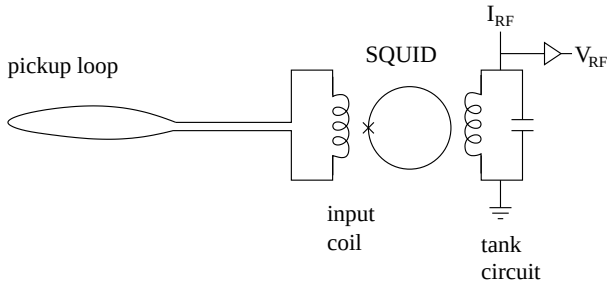

Figure 10. Simplified diagram of the electronics in an RF SQUID.

directly related to Φ, which is obtained by counting the number of voltage oscillations in the tank circuit. A schematic diagram of an RF SQUID is shown in figure 10. [74, pp. 1119–1122]

Vibrating sample magnetometer is based on an inductive method of measuring the magnetization. The sample is placed inside a pickup coil and vibrated mechanically by a piezoelectric element or a linear motor [65, pp. 57–60], so that an alternating voltage is induced in the coils. For sinusoidal vibration with amplitude A and frequency f, the induced voltage as a function of time t is

$$V_{\text{coil}}(t) = 2\pi f CMA \sin(2\pi f t), \tag{50}$$

where C is a coupling constant, derived from calibration measurements.

In this work, three types of measurements were used to study the magnetization $M(T)$ of the samples: zero-field-cooled (ZFC), field-cooled (FC), and thermoremanent magnetization (TRM) measurements. In ZFC measurement the sample was cooled in zero external magnetic field to a low starting temperature, *e.g.* 5 K, then an external field was applied and values of $M(T)$ were recorded as the temperature was raised back to the room temperature or above. FC magnetization was obtained by first switching the external magnetic field on at a starting temperature, 300 K or 460 K, and then lowering the temperature while the magnetization was recorded. Temperature dependence of TRM was studied by cooling the sample to a low temperature in an external field, switching off the field, and measuring the magnetization while raising the temperature to 300 K. Dependence of the magnetization on the external magnetic field, *i.e.* hysteresis, was studied by cooling the sample to the measurement temperature in zero field, and recording the value of $M(B)$ while the field was raised to a wanted maximum B_{max}, then in opposite direction to $-B_{max}$, and finally back to zero.

Magnetic measurements on CdSb were made with a *Cryogenic S600 XI SQUID*

magnetometer. The temperature ranges used were 5–300 K and 300–460 K, and the fields in $M(T)$ measurements were 0.005, 0.007, 0.02, 0.03, 0.05, 0.1, 0.2, 0.5, and 1 T. The $M(B)$ curves were measured in fields of $-6 \leq B \leq 6$ T and temperatures of 5, 50, 100, 200, and 300 K.

The ZFC, FC, TRM, and $M(B)$ measurements were made in the temperature range of 5 K $\leq T \leq$ 300 K. The SQUID magnetometer was also used to study the time dependence of magnetic relaxation, when the sample is first cooled in a field, then field is switched off and $M(T)$ recorded as function of "measurement time", *i.e.* the time elapsed from switching off the field. A vibrating sample magnetometer (*Quantum Design Physical Property Measurement System*) was used for $M(T)$ measurements in temperatures of 5–350 K at 100 mT magnetic field.

Ni-doped CdSb samples were oriented in the magnetometer measurements so that the external magnetic field was aligned parallel to the long edge of the sample prism. Three different samples were used, one for each of the three crystallographic directions.

2.5 Electron paramagnetic resonance measurements

When an electron with magnetic moment μ_e is placed in a homogenous external magnetic field **H**, a torque

$$\mathbf{T} = \mu_e \times \mathbf{H} \tag{51}$$

is applied on it and due to this torque [86, p. 146] the magnetic moment of the sample will precess around **H**. The magnetization density M of the sample can be written as

$$M = N\mu_e, \tag{52}$$

where N is the number of magnetic moments per unit volume. The magnetization vector will also show precession according to the equation [86, p. 147]

$$\frac{\mathrm{d}\mathbf{M}}{\mathrm{d}t} = -\gamma(\mathbf{M} \times \mathrm{H}), \tag{53}$$

where γ is the gyromagnetic ratio

$$\gamma = \frac{ge}{2m_e c}, \tag{54}$$

g is the Landé g-factor, e is the electron charge, m_e is the electron mass, and c is the speed of light.

If an alternating field **h** with angular frequency $\omega = 2\pi f$ is applied perpendicular to an external dc field $\mathbf{H}_0$, the field **H** in the equations above must be replaced with a

rotating field

$$\mathbf{H} = \mathbf{H}_i + \mathbf{h}e^{i\omega t}, \tag{55}$$

where the time-independent term $\mathbf{H}_i$ includes all dc fields, like $\mathbf{H}_0$ and any internal anisotropy fields. Assuming that the amplitude of the time-dependent field $h \ll H_i$, the magnetization is

$$\mathbf{M} = \mathbf{M}_0 + \mathbf{m}e^{i\omega t}, \tag{56}$$

with $m \ll M_0$. An expression for $\mathbf{m}$ can be derived [86, p. 149] in the form

$$\mathbf{m} = \frac{1}{\omega_0^2 - \omega^2}\left[i\omega\gamma(\mathbf{M}_0 \times \mathbf{h}) + \gamma^2(\mathbf{H}_0 \cdot \mathbf{M}_0)\mathbf{h} - \gamma^2(\mathbf{H}_0 \cdot \mathbf{h})\mathbf{M}_0\right], \tag{57}$$

where ω_0 is the electron natural precession frequency. Eq. (57) has a singularity at $\omega = \omega_0 = \gamma H_0$, which defines the electron paramagnetic resonance (EPR) condition.

EPR studies of the ceramic samples were made with an X-band ($\sim$ 9.5 GHz) EPR spectrometer and a cylindrical microwave cavity in TE_{011} mode at 100 kHz magnetic field modulation. The temperature range in the measurements was 4.2–300 K. The results were used to investigate Fe^{3+} ions at Zn positions in the host lattice. The measurements and analysis of the spectra were made by prof. L. Vlasenko at Wihuri Physical Laboratory, University of Turku.

2.6 Resistivity measurements

Resistivity measurements of the CdSb prisms were made in an He exchange gas dewar using pulsed magnetic fields up to 30 T and sample temperatures of 1.5–300 K. The magnetic field pulse length in the measurements was 8 ms. The field directions were transversal to the long axes of the samples, so that *e.g.* for the sample with the long axis in [100] direction, the magnetic field **B** is parallel to [001] and the current **j** is parallel to [100] direction. The resistivity of the samples was recorded from two different pairs of potential contacts on the samples.

3 Ni-doped CdSb: Magnetic anisotropy and hopping conductivity

3.1 Magnetization measurements and analysis

3.1.1 Zero-field-cooled and field-cooled magnetization

Measurements of ZFC and FC mass magnetizations M_{ZFC} and M_{FC}, respectively, showed anisotropic behaviour for different field orientations. The obtained values in [001] direction were considerably higher than those in [100] and [010] orientations, the latter two being roughly equal. Figure 11 presents some temperature and magnetic field dependences of ZFC and FC susceptibilities, $\chi_{ZFC} \equiv \frac{M_{ZFC}}{B}$ and $\chi_{FC} \equiv \frac{M_{FC}}{B}$, respectively.

Magnetic irreversibility, *i.e.* the separation of M_{ZFC} and M_{FC} curves, was observed even near the highest measurement temperatures for the lowest magnetic fields used. However, the onset of the irreversibility was suppressed to lower temperatures with increasing fields, and at 400 mT the irreversibility disappeared in the whole temperature range. Below 400 mT, a broad maximum in M_{ZFC} was found around 100 K. This kind of behaviour is expected for an assembly of superparamagnetic particles, as described in section 1.3.1.

3.1.2 Thermoremanent magnetization

Thermoremanent magnetization was measured at 5–300 K, with the same initial field values as in ZFC and FC measurements. The thermoremanent susceptibilities $\frac{\mathrm{TRM}(T)}{B}$ were then compared to the difference $\Delta\chi \equiv \chi_{FC} - \chi_{ZFC}$ between ZFC and FC susceptibilities measured in the same field. Some of these comparisons for all three field orientations are presented in figure 12.

Generally, $\frac{\mathrm{TRM}}{B}$ and $\Delta\chi$ curve shapes for the same field values are similar, *i.e.* $\frac{\mathrm{TRM}}{B} - \Delta\chi \approx$ constant. Both exhibit the same kind of dependence on magnetic field, with the temperature above which TRM and $\Delta\chi$ are constant decreasing as the field strength is increased. For a collection of spherical superparamagnetic clusters in low magnetic fields the relation between the different magnetizations is expected to be of the form [87]

$$M_{FC} - M_{ZFC} \approx \mathrm{TRM}. \tag{58}$$

With our samples, this is clearly not the case. A possible explanation for the deviation from eq. (58) is anisotropy in the shape of the clusters, *i.e.* they are highly non-spherical in shape [**P1**].

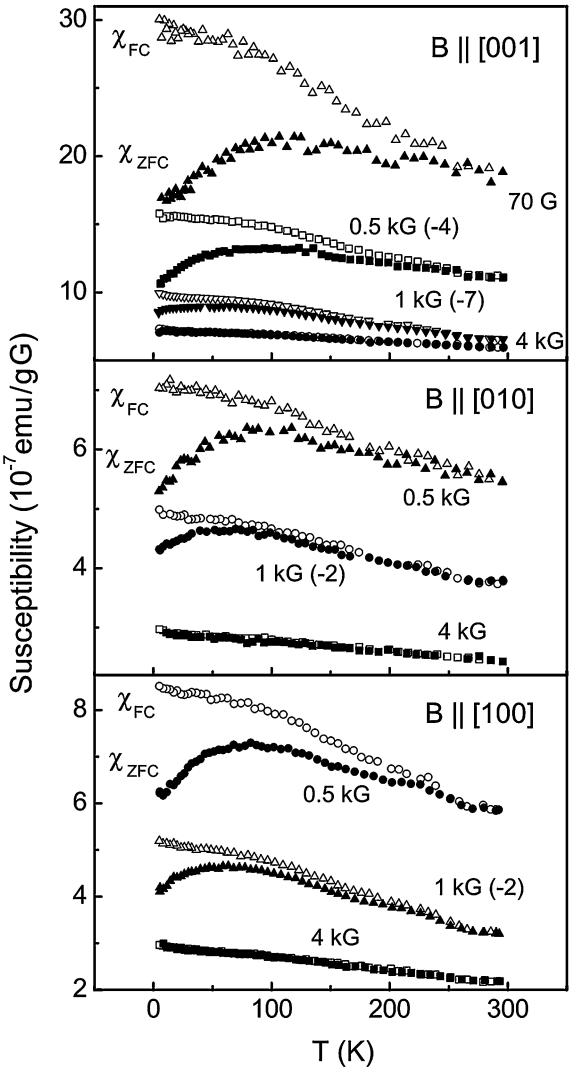

Figure 11. Temperature dependencies of χ_{ZFC} (closed symbols) and χ_{FC} (open symbols) in different magnetic fields. Some curves are shifted by the amount indicated in parenthesis (in $\frac{\text{emu}}{\text{gG}}$) for readability. [**P2**]

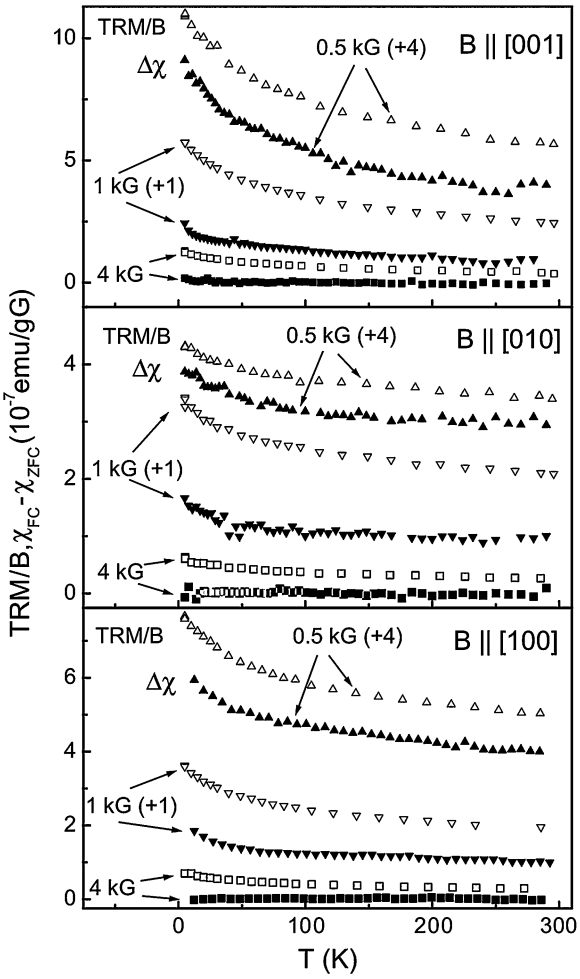

Figure 12. Temperature dependences of thermoremanent susceptibilities $\frac{\mathrm{TRM}}{B}$ (open symbols) and $\Delta\chi = \chi_{FC} - \chi_{ZFC}$ (closed symbols). For readability, some curves are shifted upwards. [**P2**]

3.1.3 Dependence of magnetization on magnetic field

Measuring the magnetization of the samples at a fixed temperature while changing the external field strength directly shows that there are coexisting diamagnetic and ferromagnetic components in the samples. The source of the diamagnetic component is expected to be the CdSb host lattice. Figure 13 presents $M(B)$ curve for [001]-oriented sample measured at 5 K, and how it is formed from the superposition of diamagnetic and ferromagnetic contributions.

The field dependence of the magnetization was qualitatively similar for all three samples, with the magnetization saturating at $B \approx 2$ T. Figure 14 presents $M(B)$ curves at four different temperatures for $B \parallel [001]$ after substraction of the diamagnetic component. The saturation magnetization is seen to decrease with increasing temperature. The inset in figure 14 shows a more detailed view of the magnetization within -150 mT $\leq B \leq 150$ mT measured at 200 K. An open hysteresis loop is clearly visible. The scattering in the data is mainly contributed to uncertainties in subtraction of the diamagnetic components.

Figure 15 presents the values of coercivity $B_c^{(j)}$, saturation magnetization $M_s^{(j)}$, and remanence $M_R^{(j)}$, where $j = 1$, 2, and 3 corresponding to the magnetic field orientation along [100], [010], and [001] axes, respectively, measured at different temperatures. As with M_{ZFC} and M_{FC}, both the saturation magnetization and remanence are anisotropic with comparable values in [100] and [010] orientations, and considerably higher values observed for $B \parallel [001]$ configurations. Coercivity shows a different kind of anisotropy, as $B_c^{(3)} < B_c^{(2)} < B_c^{(1)}$. Non-zero coercivities are observed at all temperatures used in our measurements. [**P1**–**P3**]

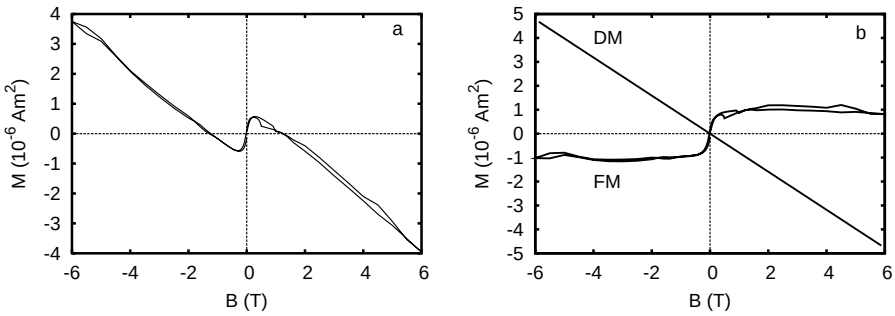

Figure 13. a) $M(B)$ curve of [001]-oriented sample measured at 5 K. b) $M(B)$ curve separated into its diamagnetic (DM) and ferromagnetic (FM) components.

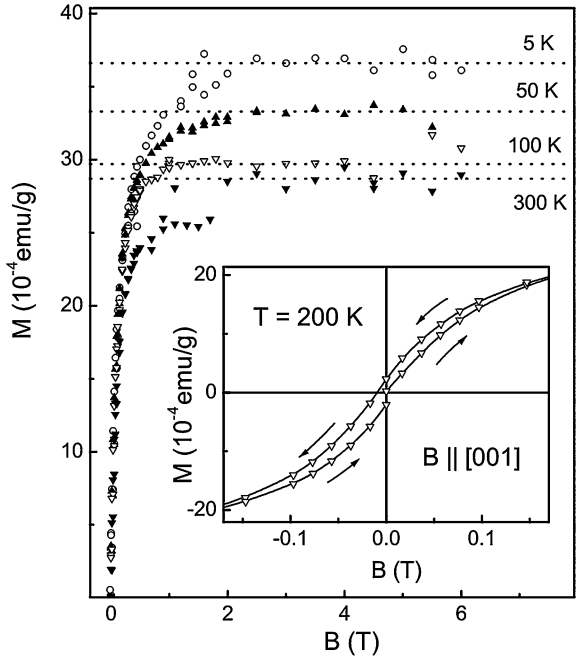

Figure 14. Magnetic field dependence of magnetization for $B \parallel [001]$ at four different temperatures. The dashed lines are the estimates for the saturation levels. Inset: Hysteresis loop measured at 200 K. The arrows indicate the increasing and decreasing field directions. [**P2**, **P3**]

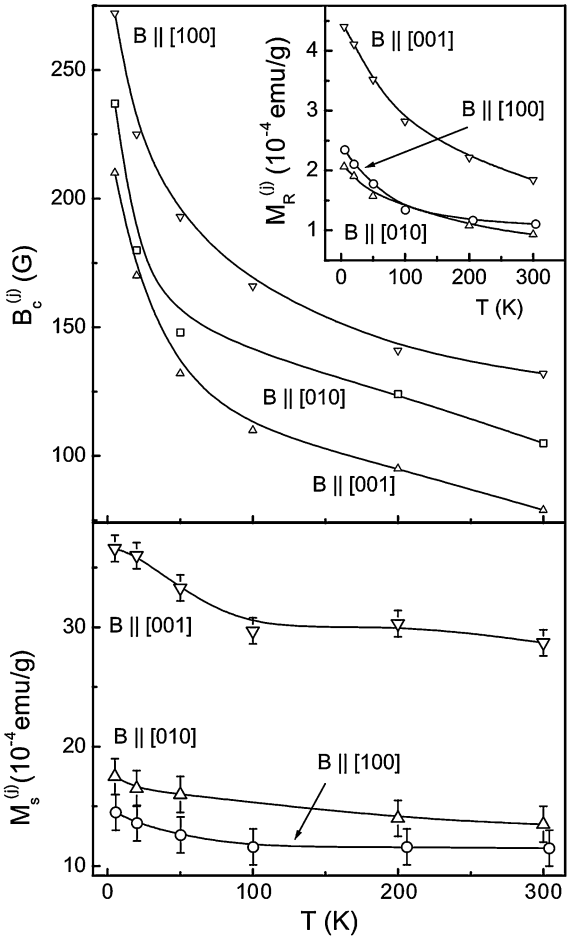

Figure 15. Temperature dependences of coercivity $B_c^{(j)}$ (upper panel), saturation magnetization $M_s^{(j)}$ (lower panel), and remanence $M_R^{(j)}$ (inset in the upper panel). The lines are guides to the eye. [**P1**, **P2**]

3.1.4 Superparamagnetism

The measured blocking temperatures, T_b, followed the expected magnetic field dependence in eq. (7). Figure 16 presents the blocking temperatures determined from the maxima in ZFC curves as a function of the magnetic field, and linear fits to the data points. The blocking temperatures did not show any clear dependence on the field orientation, and so the parameters obtained from the linear fits with eq. (7) are close to isotropic. Values of $T_b(0)$ and the mean anisotropy field, B_{K}, determined from the fits are presented in table 2. These parameters were used to calculate the mean magnetic moments of the clusters μ, which are also presented in table 2. The cluster moment values are typical for nanosized magnetic particles [88–90].

Estimations of the coercive field values at zero temperature, $B_c^{(j)}(0)$, were made by fitting eq. (12) to the measured $B_c^{(j)}(T)$ data, testing different n values. Only the lowest temperatures provided some success for these fits, with $n = \frac{2}{3}$, *i.e.* magnetization reversal by curling, giving the best fits at 5–20 K. These fits and the data points are presented in figure 17. The obtained values for $B_c^{(j)}(0)$ are shown in table 3. A likely explanation for the deviation from the theory is an inhomogeneity in the orientation, aspect ratio, and size of the magnetic clusters in the samples.

The coercivity data can be used for estimating the angles θ_j in section 1.3.1. Using eq. (22) with $B_c^{(0)}$ values obtained above, and assuming $X \ll Y$ in eq. (21), we get $\cos^2\theta_j \approx \frac{1}{Z_j}$, from which the values of the angles can be calculated. These are presented in table 3 as $\theta_j^{(B)}$, with the calculated values of Z_j.

Another option for estimating the angles θ_j is to use the saturation magnetization data. Ratios of $\frac{M_s^{(j)}(0)}{M_s^{(i)}(0)}$ for $i \neq j$ are written with eq. (17), assuming that the zero temperature ratios for the saturation magnetizations approximately follow the ratios measured at 200 K. These simultaneous equations are combined with the constraint equation (15), and solved numerically to get the values for $\theta_j^{(M)}$ in table 3.

The distributions of θ_j angles around their mean values $\theta_j^{(B)}$ and $\theta_j^{(M)}$ are estimated by the conversion $\theta_j \to \theta_j + \alpha_j$ in eqs. (15)–(17). α_j is a random deviation around the mean angle, constrained by $-\Delta_j < \alpha_j < \Delta_j$, where Δ_j is the width of the distribution. The distribution function $f(\alpha_j)$ is approximated with a step function

$$f(\alpha_j) = \begin{cases} \frac{1}{4\Delta\varphi_j \Delta_j \sin\theta_j} & \text{if } -\Delta_j < \alpha_j < \Delta_j \\ 0 & \text{if } |\alpha_j| \geq \Delta_j, \end{cases} \tag{59}$$

where $\Delta\varphi_j$ is the distribution of the polar angle φ_j around the jth axis. The mean value of magnetization, $\langle M_s^{(j)}(0)\rangle$, is obtained by averaging over the angular distribution:

Table 2. The values of zero-field blocking temperature $T_b(0)$, anisotropy field B_K, and the mean cluster magnetic moment μ for CdSb doped with Ni.

Orientation	$T_b(0)$ (K)	B_K (mT)	μ (10^4 μ_B)
$B \parallel [100]$	107 ± 5	390 ± 50	2.0 ± 0.2
$B \parallel [010]$	105 ± 5	470 ± 50	1.7 ± 0.2
$B \parallel [001]$	110 ± 3	450 ± 50	1.8 ± 0.2

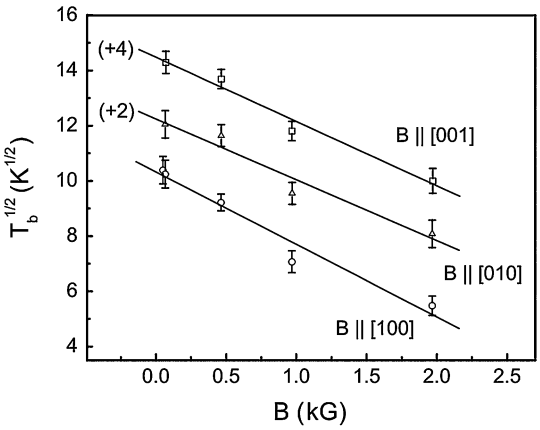

Figure 16. Dependence of $T_b^{\frac{1}{2}}$ on external magnetic field from measured data (points), and linear fits to the data points (lines). Plots for $B \parallel [010]$ and $B \parallel [001]$ orientations are shifted upwards by the values indicated in parenthesis (in $K^{\frac{1}{2}}$) for clarity. [**P2**]

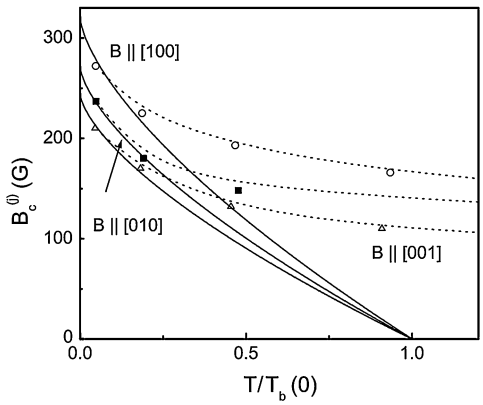

Figure 17. Measured coercivity values $B_c^{(j)}(T)$ as a function of $\frac{T}{T_b(0)}$ (points), and fits of eq. (12) with $n = \frac{2}{3}$ (solid lines) to the data points. Dashed lines are guides to the eye. [**P2**]

$$\begin{aligned}
\langle M_s^{(j)}(0)\rangle &= \int M_s^{(j)}(0)\, f(\alpha_j)\mathrm{d}\Omega \\
&= \frac{\eta M_s^*}{4\Delta\varphi_j\Delta_j\sin\theta_j}\int_{\varphi_j-\Delta\varphi_j}^{\varphi_j+\Delta\varphi_j}\mathrm{d}\varphi_j\int_{-\Delta_j}^{\Delta_j}\mathrm{d}\alpha_j \\
&\quad\times\left[1-D_c-(D_c-D_a)\cos^2(\vartheta_j+\alpha_j)\right]\cos(\vartheta_j+\alpha_j)\sin(\vartheta_j+\alpha_j) \\
&= \frac{\eta M_s^*}{2\Delta_j}\sin(2\Delta_j)\cos(\vartheta_j) \\
&\quad\times\left[1-D_c-(D_c-D_a)(\cos^2\Delta_j\cos^2\vartheta_j+\sin^2\Delta_j\sin^2\vartheta_j)\right]. \qquad (60)
\end{aligned}$$

The mean values of the coercivities, $\langle B_c^{(j)}\rangle$, are obtained similarly. Using $X \ll Y$, the expression found in [**P2**] is

$$\langle B_c^{(j)}\rangle = \frac{2\pi M_s^* X^{1/2}}{2\Delta_j\sin\vartheta_j}\ln\frac{1+\tan\Delta_j\tan\vartheta_j}{1-\tan\Delta_j\tan\vartheta_j}. \qquad (61)$$

Eqs. (60) and (61) can be solved by using the ratios of $\frac{\langle M_s^{(i)}(0)\rangle}{\langle M_s^{(j)}(0)}\rangle$ and $\frac{\langle B_c^{(i)}(0)\rangle}{\langle B_c^{(j)}(0)}\rangle$, where $i \neq j$, to obtain the widths of the distributions, $\Delta_j^{(M)}$ and $\Delta_j^{(B)}$, respectively. These values are presented in table 3.

Other parameters related to superparamagnetism can be obtained by neglecting the variance in θ_j, *i.e.* $\theta_j \approx \vartheta_j$. Using $\eta = NV$ and $\mu = M_s^* V$ in eqs. (17) and (19), the

Table 3. Calculated values of coercivities at 0 K $B_c^{(j)}(0)$, parameters Z_j, the mean angles $\theta_j^{(B)}$ and $\theta_j^{(M)}$, and their angular distributions, $\Delta_j^{(B)}$ and $\Delta_j^{(M)}$, respectively. [**P2**]

Orientation	$B_c^{(j)}(0)$ (mT)	Z_j	$\theta_j^{(B)}$ (°)	$\Delta_j^{(B)}$ (°)	$\theta_j^{(M)}$ (°)	$\Delta_j^{(M)}$ (°)
$B \parallel [100]$	32.0	4.13	60	3	66	3
$B \parallel [010]$	27.1	2.95	54	4	62	5
$B \parallel [001]$	24.4	2.93	49	7	39	6

concentration of the clusters, N, can be calculated from

$$N = \frac{\sum_{j=1}^{3} \frac{M_s^{(j)}(0)}{\cos\theta_j^{(M)}}}{2\mu}, \tag{62}$$

which gives $N \approx 1.8 \cdot 10^{14}\ \frac{\text{clusters}}{\text{cm}^3}$. The mean intercluster distance, $\langle R \rangle$, can then be approximated using the Wigner–Seitz radius [91, p. 4] $r_s = \left(\frac{4\pi N}{3}\right)^{-1/3}$. For a collection of randomly distributed clusters, $\langle R \rangle = 2r_s$, yielding $\langle R \rangle \approx 240$ nm.

If most of the Ni ions in the samples are used in forming the magnetic phase, the volume fraction of the magnetic phase η is approximately $3.8 \cdot 10^{-3}$. The mean number of Ni ions per cluster, n_{ion}, is then calculated from $n_{\text{ion}} = \frac{\eta N^*}{N}$, where N^* is the Ni ion concentration in pure Ni ($9.1 \cdot 10^{22}$ cm^{-3}), yielding $n \approx 1.8 \cdot 10^6$. The average magnetic moment per Ni ion, μ_{ion}, is then $\frac{\mu}{n_{\text{ion}}} \approx 0.01\mu_{\text{B}}$.

The saturation magnetization at 0 K, M_s^*, is roughly 500 $\frac{\text{emu}}{\text{cm}^3}$ for bulk Ni [92], and 350 $\frac{\text{emu}}{\text{cm}^3}$ for $\text{Ni}_{1-x}\text{Sb}_x$, where $x = 0.038$ [55, p. 162]. The mean cluster radius, r, can be estimated from equation

$$r = \left(\frac{3M_s^*}{4\pi m\mu}\right)^{1/3}. \tag{63}$$

$\frac{\kappa}{S^2}$ is solved from eq. (16), and the exchange stiffness constant A is estimated with equation

$$A = 2\pi\left(\frac{M_s^* \frac{\kappa}{S^2} r}{q}\right)^2. \tag{64}$$

Single-domain particle radii r_{sd} and critical radii r_c are then calculated with eqs. (10) and (11), respectively. The volume fraction η^{calc} is obtained from equation $\eta^{\text{calc}} = \frac{G}{2M_s^*}$, where $G = \sum_{j=1}^{3} \frac{M_s^{(j)}(0)}{\cos\theta_j^{(M)}}$, and the magnetization per Ni ion is calculated from $\mu_{\text{ion}}^{\text{calc}} = \frac{\mu_{\text{ion}}\eta}{\eta^{\text{calc}}}$. The equations above are used for evaluating the parameters in two ways. First, a fixed value $m = 4$ is used with the limiting values of M_s^*. Second, M_s^* is fixed to 430 $\frac{\text{emu}}{\text{cm}^3}$,

Table 4. Estimated parameters for superparamagnetic clusters: Cluster radius r, single-domain radius r_{sd}, critical cluster radius r_c, cluster volume fraction η, and magnetization per Ni ion in the clusters μ_{ion}. [**P2**]

Parameter	Fixed m	Fixed M_s^*	Experimental
r (nm)	2.8–3.1	1.9–3.2	–
r_{sd} (nm)	115–130	70–135	–
r_c (nm)	1.6–1.8	0.4–2.2	–
η	$(0.6-0.9)\cdot 10^{-4}$	$0.8\cdot 10^{-4}$	$3.8\cdot 10^{-3}$
$\mu_{\text{ion}}(\mu_{\text{B}})$	0.4–0.6	0.5	0.01

and m is varied between 3 and 15. The results of these calculations are presented in table 4, with some experimental values obtained in the section above.

3.1.5 Discussion

The temperature dependences of χ_{ZFC} and χ_{FC} in figure 11, along with the dependence of T_b on external field are typical for coherent rotation of the magnetization of superparamagnetic clusters. However, the anisotropies of the saturation magnetization and the coercivity would rather point to reversal by curling for an assembly of spheroidal clusters oriented around a preferred direction. This contradiction is reconciled by comparing the estimated values of r to r_{sd} and r_c in table 4. For $m \geq 4$, the angles φ_j coincide with θ_j. Then, for an upper limit of $m < 6-8$, we have $r \ll r_{sd}$, but also $r \sim r_c$. The broad maximum in χ_{ZFC} curves points to a wide distribution of cluster sizes in our samples; thus, a wide cross-over region between the two reversal modes can be expected, which explains the observed behaviour.

The large difference between the calculated and experimental values of μ_{ion} in table 4 suggests that only a small portion of Ni enters the clusters. The experimental value of 0.01 μ_{B} per Ni ion is considerably lower than the smallest value for ferromagnetic $Ni_{1-x}Sb_x$, 0.24 μ_{B} per ion [55, p. 440]. An estimate of the Ni fraction in the clusters can be made from the ratio $\frac{\eta}{\eta^{\text{calc}}}$, which gives 1.7–2.4 % for limiting values of M_s^* [**P2**]. The rest of Ni are expected to form a paramagnetic subsystem with small magnetic moments, which can explain the stronger temperature dependence of the saturation magnetization at low temperatures, as seen in figure 15. To minimize the effect of this paramagnetic system, our analysis above used the values of M_s at 200 K instead of low-temperature

values.

As shown on page 232 in publication **[P2]**, angles θ_j follow the relation $\theta_1 > \theta_2 > \theta_3$ for both $\theta_j^{(B)}$ and $\theta_j^{(M)}$. While the values of $\theta_j^{(B)}$ and $\theta_j^{(M)}$ differ by some 10–20 % for the same j, they have an overlapping interval when the estimated widths of the angle distributions Δ_j are taken into account. The demagnetization factors calculated for prolate spheroids with the parameters obtained above suggest only a small corrections to $\theta_j^{(M)}$ values [**P2**].

The interactions between the clusters are estimated as follows: The large mean distance between the clusters, $\langle R \rangle \approx 240$ nm prohibits direct interactions between Ni ions in the different clusters. Assuming that the free carrier concentration n_f is similar to undoped CdSb, $n_f \sim 10^{15}$ cm^{-3} at room temperature [25], and an exponential decrease of n_f with lowering temperature, the free carrier concentration is too low at the lower temperatures to allow RKKY interaction mediated by the free carriers. An estimate of dipolar interaction energy, W_d between the clusters can be made using the approximation $W_d \approx \frac{z_J \mu^2}{R^3}$, where $z_J \approx 33$ [93], yielding $W_d \sim 0.1$ meV. This is three orders of magnitude lower than the anisotropy energy $KV \sim 100$ meV, so the dipolar interaction is negligible in the blocking of moments.

3.2 Electrical resistivity

3.2.1 Resistivity in zero magnetic field

The temperature dependence of the resistivity of a semiconductor exhibiting thermal activation of carriers from shallow impurity levels to conduction or valence bands follows an exponential law [77, pp. 75–76]

$$\rho(T) = \rho_0 e^{\frac{E_A}{k_B T}}, \tag{65}$$

where ρ_0 is a prefactor and E_A is activation energy. Thus, the activation energy can be obtained from experimental data by plotting $\ln\rho$ versus $\frac{1}{T}$, and fitting eq. (65) to the plots. In reality, the values of E_A obtained in this manner are approximate, as ρ_0 depends on the temperature too, due to the mobility of the charge carriers [77, p. 76]. The values of ρ_0 and E_A derived from fits to linear parts of the data at 5–20 K are presented in table 5.

To analyze the hopping conductivity, eq. (40) is written in the form [76]

$$\ln\left(\frac{E_a}{k_B T} + m\right) = \ln p + p\ln T_0 + p\ln\frac{1}{T}, \tag{66}$$

where $E_a \equiv \frac{\mathrm{d}\ln\rho}{\mathrm{d}\frac{1}{k_B T}}$ is the local activation energy [77, p. 208]. Then $\frac{E_a}{k_B T} + m$ is plotted versus $\ln\frac{1}{T}$, and linear fits with fixed m values of $\frac{1}{4}$, $\frac{1}{2}$, and 1 are tested to find out which one yields $p \approx m$. The fits and the values of m and p are presented in figure 18. Below $T \approx 2.5$ K, the best fits for samples 1 and 3 correspond to p values of $\frac{1}{2}$, which means the SE VRH mechanism. The situation is different for sample 2, for which $p = \frac{1}{4}$ at $T \approx$ 1.8–2.5 K points to Mott VRH. [**P3**]

Another way to analyze the resistance data is to plot $\ln\frac{\rho}{T^p}$ versus T^{-p}, with $p = \frac{1}{4}$, $\frac{1}{2}$, and 1. Linear fits to the plots with different p can then be used to determine the main hopping type by comparing the temperature ranges where the fits approximate the data well. Figure 19 presents the plots for samples 1–3 with $p = \frac{1}{2}$, and the linear fits. These fits represent the best matches to samples 1 and 3; however a better fit for sample 2 is obtained by using $p = \frac{1}{4}$, presented in figure 20. From these considerations, the results relating to figure 18 are replicated: SE VRH ($p = \frac{1}{2}$ in eq. (40)) gives the best fit for samples 1 and 3, while Mott VRH is realized for sample 2. No NNH conductivity was observed in any of the samples. [**P3**]

Table 5. Values of the parameters obtained from fits to experimental data on 2 at.-% Ni-doped CdSb [84, **P3**]. The long edge crystallographic direction (*i.e.* the direction of **j** in the measurement) is presented with the sample number, ρ_0 is the prefactor, E_A is the activation energy in eq. (40), p is the exponent in eq. (40) used in the fit and D is the prefactor, and T_0 is the characteristic temperature.

Sample	ρ_0 (Ω cm)	E_A (meV)	p	D (Ω cm K^{-p})	T_0 (K)
1, [100]	0.0378	2.45	1/2	0.491	18.7
2, [010]	0.0475	2.50	1/4	0.0928	3180
3, [001]	0.0111	2.85	1/2	0.477	51.3

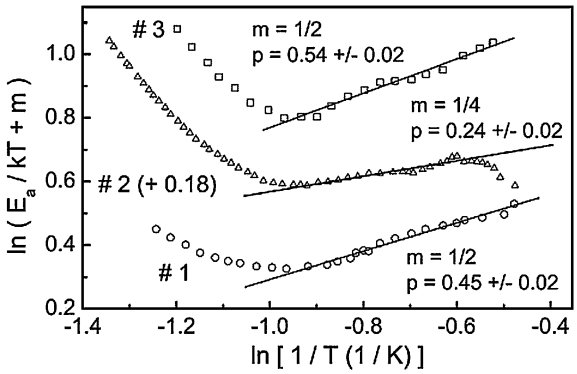

Figure 18. $\ln\left(\frac{E_a}{k_B T} + m\right)$ plotted versus $\ln\frac{1}{T}$ (points), and linear fits to data points (lines). Selected values of m, and values of p obtained from the fits are also presented. Data points of 2 at.-% Ni-doped CdSb sample 2 (#2) are shifted upwards for clarity. [**P3**]

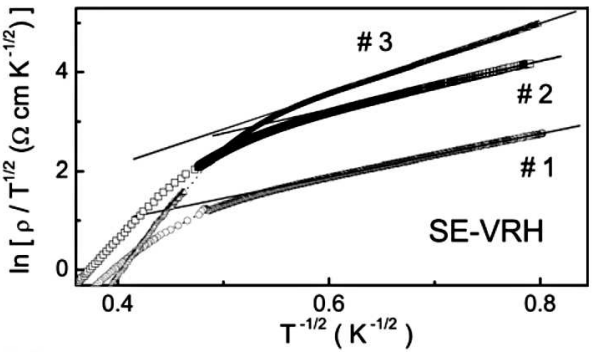

Figure 19. $\ln \frac{\rho}{T^{1/2}}$ plotted versus $T^{-1/2}$, and linear fits to data points fitted for the samples #1, #2, and #3 with $p = \frac{1}{2}$. [**P3**]

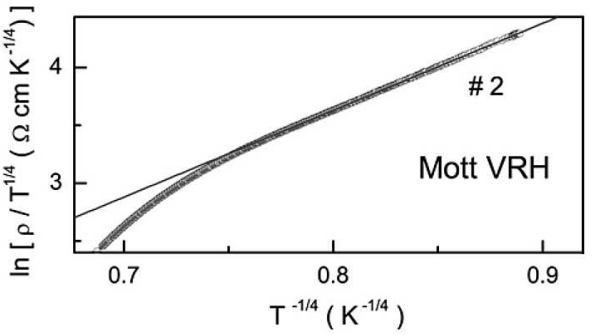

Figure 20. $\ln \frac{\rho}{T^{1/4}}$ plotted versus $T^{-1/4}$ for sample 2, and linear fits to data points. [**P3**]

3.2.2 Magnetoresistance in the weak field limit

Quadratic behaviour of the field dependence of MR in the weak field limit is expected for hopping conductivity, as given in eq. (41). Figure 21 presents plots of $\ln\rho$ as function of B^2 for samples 1–3, and linear fits to data points. As can be seen from this figure, the linear regime extends up to $B \approx 5$–6 T.

The slopes of the linear fits for sample 2 are constant between 3 and 4.2 K, and increase a little below 3 K. Normalizing ρ with the measured zero field values $\rho(0)$ as in eq. (41), the slope of $C_{ex}^{(2)} = (4.49 \pm 0.04) \cdot 10^{-2}$ T^{-2} is found for 3 K and 4.2 K fits. For sample 3, all the slopes in this temperature range are constant, with $C_{ex}^{(3)} = (6.41 \pm 0.04) \cdot 10^{-2}\mathrm{T}^{-2}$. [84, **P3**]

The data on sample 1 of CdSb containing Ni-rich nanoclusters in figure 21 shows the slope varying with temperature. Marking the slopes with A_{ex}, we find that $A_{ex}(T) = A_{ex}^{(0)} T^{-\frac{3}{4}}$, with $A_{ex}^{(0)} = (6.7 \pm 0.1) \cdot 10^{-2}$ T^{-2}K$^{3/4}$. The temperature dependence of A_{ex} is presented in figure 22. [84, **P3**]

Samples 1 and 2 also show a slight deviation from the linear behaviour in the lowest fields, indicating an additional negative MR. This can be explained by quantum interference that affects the paths associated with hopping between two potential wells [94]. However, the effect is small in our samples, and analysis [84] shows that it is expected to vanish at 0.7 T, so the effect is neglected.

The dominant hopping type in the weak field limit can be determined by comparing the temperature dependences of the measured slope values to eqs. (42)–(45). The constant slope value for sample 3 and the near-constant values for sample 2 at 1.5–4.2 K suggest that NNH is the main hopping process in these samples. At the same temperature range, Mott VRH describes the hopping in sample 1, as for Mott VRH $\ln\left[\frac{\rho(B)}{\rho(0)}\right] \propto T^{-3/4}B^2$. Table 6 summarizes the observations of the different hopping types for all three samples in zero external field, and at the weak field limit.

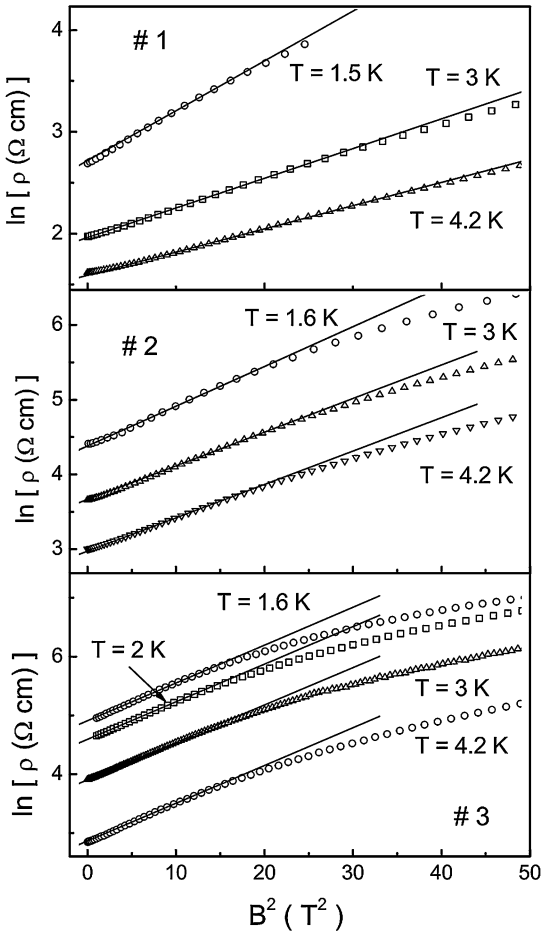

Figure 21. $\ln\rho$ plotted versus B^2, and linear fits to experimental data. [**P3**]

Table 6. Summary of the observed hopping types in zero external field, and at the weak field limit. The different hopping conductivity types are Mott variable-range hopping (Mott VRH), Shklovskii–Efros variable-range hopping (SE VRH), and nearest-neighbour hopping (NNH). [**P3**]

	Hopping type	
Sample	$B = 0$ T	Weak field limit
1	SE VRH	Mott VRH
2	Mott VRH	NNH
3	SE VRH	NNH

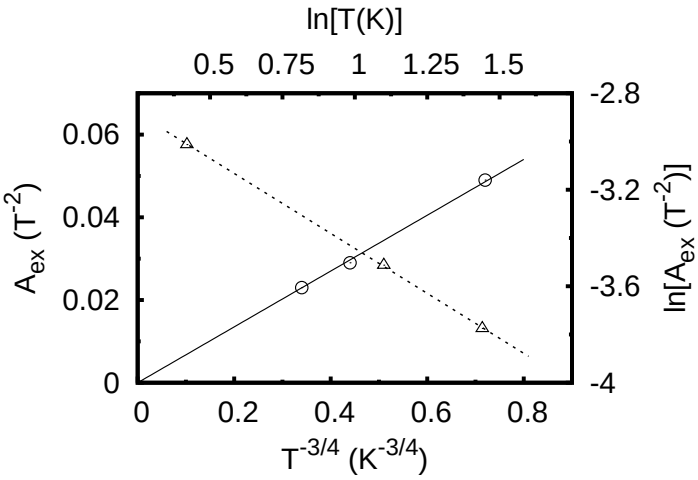

Figure 22. Temperature dependence of the slopes A_{ex} in linear fits to $\ln\rho$ vs. B^2 data in figure 21 for sample 1: A_{ex} vs. $T^{-3/4}$ (circles) and $\ln A_{ex}$ vs. $\ln T$ (triangles). The lines are linear fits. [**P3**]

3.2.3 Microscopic parameters

Several microscopic parameters relating to hopping conductivity can be determined by resistivity measurements in zero field and weak field limits. From the zero-field data, the Coulomb gap widths Δ for samples 1 and 3 are estimated with the expression [95, 96]

$$\Delta = \frac{k_{\mathrm{B}}}{2}\sqrt{T_{0SE}T_v}, \tag{67}$$

where T_v is the onset temperature for SE VRH. From figure 18, $T_v \approx 2.5$ K, while the experimental value of $p = 0.24$ agrees well with $\frac{1}{4}$ predicted for the Mott VRH. For the two samples 1 and 3, the relative permittivity ε_r can be found using the approximations [84]

$$\Delta \approx U = \frac{e^2}{\varepsilon_r R_{\mathrm{h}}}, \tag{68}$$

where U is the energy of the Coulomb repulsion between the mean distance

$$R_{\mathrm{h}} \approx 2\left(\frac{4\pi}{3eR_{77}}\right)^{1/3}, \tag{69}$$

where R_{77} is the Hall coefficient at 77 K. The density of states (DOS) outside the Coulomb gap, g_0, is calculated from the equation [97]

$$g_0 = \frac{3\varepsilon_r^3\Delta^2}{\pi e^6}. \tag{70}$$

As the DOS parameters for VRH are usually close to each other [96], the density of the localized states g can be evaluated from $g \approx g_0$. The localization radius a is then calculated from eq. (38).

The anisotropy coefficient p_3 for sample 1 can be calculated with the determined value of A_{ex} at the weak field limit. This is done by setting $A_{ex} = A_{03}^{(M)}$ in eq. (44), and using the value of a (mean distance between magnetic ions) obtained above to calculate p_3.

The acceptor concentration N_a for sample 3 can be solved as function of p_2 from eq. (43) by setting the experimental value $C_{ex}^{(3)}$ equal to C_2. The DOS is approximated with a rectangular function, with the width of the DOS, W, given by

$$W = \frac{N_a}{2g_0} + \frac{2}{3}\Delta, \tag{71}$$

and from this equation W for sample 3 is solved as function of p_2.

Near a metal-insulator transition (MIT), the localization radius and the dielectric permittivity follow the scaling laws [98]

$$a = a_0 \left(1 - \frac{N_a}{N_c}\right)^{-\nu} \tag{72}$$

and

$$\varepsilon_r = \varepsilon_{r0} \left(1 - \frac{N_a}{N_c}\right)^{-\zeta}, \tag{73}$$

where N_c is the critical acceptor concentration, and ν and ζ are the critical exponents for a and ε_r, respectively. These equations can be used to solve the ratio between the critical exponents, using the values obtained for samples 1 and 3 above:

$$\frac{\zeta}{\nu} = \frac{\ln[\varepsilon_r(\text{Sample1})/\varepsilon_r(\text{Sample3})]}{\ln[a(\text{Sample1})/a(\text{Sample3})]}, \tag{74}$$

which yields $\frac{\zeta}{\nu} = 1.90$.

As sample 2 exhibits Mott VRH, where the Coulomb repulsion is not a dominant effect, the calculations above cannot be used to determine the microscopic parameters for it. Setting $\Delta = 0$ in eq. (71), we get $W = \frac{N_a}{2g_0}$. This approximation leads [77, pp. 202–215] to $W \approx k_\mathrm{B} T_{\nu M}^{3/4} T_{0M}^{-1/4}$, where $T_{\nu M}$ is the onset temperature for Mott VRH. Now, as p_3 is already known, and $p_1 = \frac{1}{p_2 p_3}$, N_a and a for sample 2 can be solved as function of p_2 by setting the experimental value $C_{ex}^{(2)}$ equal to C_1 in eq. (43). Writing a set of simultaneous equations from eq. (72) for N_c of samples 2 and 3, p_2 is then varied until both equations produce the same value for N_c. The result is checked using eq. (73) for

Table 7. Microscopic parameters: Acceptor concentration N_a, localization radius a, relative permittivity ε_r, Coulomb gap width Δ, acceptor band width W, and the density of the localized states g. [**P3**]

Sample	N_a (10^{16} cm^{-3})	a (Å)	ε_r	Δ (meV)	W (meV)	g (10^{16} cm^{-3}meV^{-1})
1	3.61	196	127	0.30	0.50	5.94
2	3.37	180	108	0.18	1.28	1.31
3	2.51	139	66	0.49	0.91	2.16

Table 8. Orientation of the magnetic field j in respect to the electric current direction in eqs. (42)–(45), experimental anisotropy coefficient p_j, and calculated anisotropy coefficient $p_j^{(\mathrm{cal})}$ [**P3**].

Sample	j	p_j	$p_j^{(\mathrm{cal})}$
1	3	0.839	0.839
2	1	1.008	0.897
3	2	1.182	1.327

sample 3 to compare its value to the earlier ε_r value obtained with eq. (68). The N_c value determined in this way was $6.275 \cdot 10^{16}$ cm^{-3}.

Finally, N_a for sample 1 is calculated from eq. (72) or eq. (73), and W is obtained from eq. (71). Eq. (73) is used to find κ for sample 2, and its W value is estimated with eq. (70). The values of all the microscopic parameters are presented in tables 7 and 8. The exact steps for obtaining these parameters can be found in [84].

The microscopic parameter values agree well with the conclusions made on the hopping conductivity types based directly on experimental data: Δ is comparable to W for samples 1 and 3, while for sample 2 we find $\Delta \ll W$, as is expected for SE VRH and Mott VRH, respectively. The use of the scaling model near MIT is justified by the closeness of the ratio $\frac{\zeta}{\nu}$ to its theoretical value 2 [95], and by the values of N_a being close to the critical value N_c. [**P3**]

4 Structural and magnetic properties of ZnO doped with Fe and Mg

4.1 X-ray and atomic force microscopy measurements

4.1.1 Particle sizes and impurity phases of $Zn_{1-x}Fe_xO$

Particle sizes of $Zn_{0.94}Fe_{0.06}O$ precursor powders prepared at different temperatures were determined with the Scherrer formula (47) from x-ray diffractograms, using the (100), (102), and (110) diffraction peaks for measuring the FWHM value σ. The results are shown in table 9. Increasing average particle size with increasing sample preparation temperature is expected, as higher temperatures allow small particles to fuse into larger particles [99]. As the ceramic samples used for magnetometer measurements were sintered a second time after pressing the powder into blocks, their particles are expected to be larger than those measured from the precursor powders.

A minority phase was observed in all $Zn_{1-x}Fe_xO$ samples, as their diffractograms contained extra peaks in comparison with pure ZnO control sample. The peak positions indicate that the second phase is most likely either $ZnFe_2O_4$ or Fe_3O_4, which have similar crystal structures and bulk lattice parameters, 8.443 Å [100] and 8.396 Å [101], respectively. Using eq. (46) to estimate the peak positions for the two compounds gives less than 0.1° separation, so taking into account the peak broadening and other possible errors in the measurement it is impossible to differentiate between the second phase components in our measurements. A comparison between pure ZnO and $Zn_{0.94}Fe_{0.06}O$ diffractograms is presented in figure 23. Two small peaks at 43.3° and 50.4° can also be observed, but they originate from the copper-made sample holder. Cu has a face-centered cubic (FCC) crystal structure with lattice parameter 3.615 Å [102].

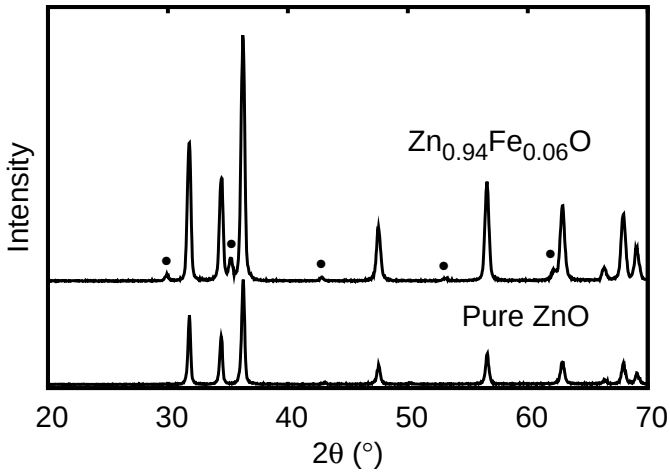

Figure 23. X-ray diffractograms of pure ZnO and $Zn_{0.94}Fe_{0.06}O$ samples. The extra peaks marked with dots in the $Zn_{0.94}Fe_{0.06}O$ diffractogram show presence of an impurity phase. The diffractogram of $Zn_{0.94}Fe_{0.06}O$ has been shifted upwards for clarity.

Table 9. Calculated average particle sizes in $Zn_{1-x}Fe_xO$ precursor powders.

Preparation temperature (°C)	Size average (nm)
500	10–14
700	25–32
1000	35–45

4.1.2 $\mathbf{Zn_{1-x-y}Fe_xMg_yO}$

X-ray diffraction measurements showed that the impurity phase observed in $Zn_{1-x}Fe_xO$ samples was not present in observable quantities in our $Zn_{1-x-y}Fe_xMg_yO$ powder samples with $y \geq 0.10$. However, the impurity peaks were present in the samples with $y = 0.02$. The x-ray results for the samples made via solid-state reaction were similar to sol-gel method samples, with no peaks in the diffractograms originating from unreacted Fe_2O_3.

A separate compound could be detected in large amounts in $Zn_{0.7}Fe_{0.04}Mg_{0.26}O$ samples. The observed peaks fit well the peaks of pure MgO which has cubic crystal structure with lattice parameter $a = 4.213$ Å [103]. As the highest reported [104] terminal solid solubility values of MgO in ZnO are only 12 mol.-%, it is clear that the impurity is MgO which was not dissolved into the main phase structure. Two typical x-ray diffractograms measured from these samples are presented in figure 24, and a calculated diffractogram for MgO is shown to help identifying the impurity phase peaks present in $Zn_{0.7}Fe_{0.04}Mg_{0.26}O$ sample.

As shown by atomic force microscopy, the surfaces of the samples consist of roughly spherical particles ranging from 200 to 800 nm. The average particle sizes were between 300 and 400 nm. Figure 25 shows a typical AFM surface image of ceramic $Zn_{0.7}Fe_{0.04}Mg_{0.26}O$ showing an average particle size of ≈ 340 nm. The particle sizes were considerably larger than those measured with x-ray diffraction from the precursor powders, which can be explained by particles fusing together during sintering of the pellets.

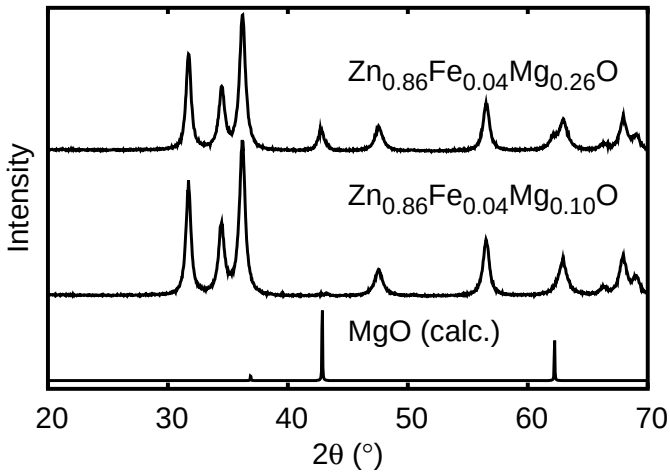

Figure 24. X-ray diffractograms of $Zn_{0.7}Fe_{0.04}Mg_{0.26}O$ and $Zn_{0.86}Fe_{0.04}Mg_{0.10}O$, and a calculated diffractogram for pure MgO. The measured diffractograms have been shifted upwards in intensity for clarity.

Figure 25. Atomic force microscopy image of the surface of ceramic $Zn_{0.7}Fe_{0.04}Mg_{0.26}O$ sample. The image size is $5 \times 5\ \mu m^2$. [**P4**]

4.2 Magnetic measurements

4.2.1 Magnetization vs. Fe content of $Zn_{1-x}Fe_xO$

Qualitative shapes of measured $M(T)$ curves were similar for all our $Zn_{1-x}Fe_xO$ samples: a peak at 15 K, and decrease of magnetization at temperatures above 15 K following the Curie–Weiss law [65, p. 8]

$$\chi = \frac{C}{T - \theta_p}, \tag{75}$$

where C is the Curie constant, with two paramagnetic Curie temperatures θ_p corresponding roughly to the temperature intervals 15 K $< T <$ 100 K and $T >$ 150 K. The maximum at 15 K is consistent with the results reported for $ZnFe_2O_4$ having the magnetic phase change at 10 K [105], and combining these results with the x-ray data, it is likely that $ZnFe_2O_4$ is present as a secondary phase in these samples.

The magnetization was found to be strictly proportional to the Fe content x in the sample. Scaling the measured magnetization by x, the results obtained for the samples with different x are similar to those in figure 26, where the ZFC magnetizations of the samples with $x = 0.01, 0.06,$ and 0.25 are plotted as a function of temperature. These results show that the amount of the secondary phase is proportional to Fe content, and that the magnetization is proportional to the amount of the secondary phase in the sample.

The dependence of $M(B)$ on the applied magnetic field is similar for all samples. Above 15 K, a narrow range of non-linear behaviour near zero field was detected, followed by a linear increase of the magnetization with increasing field, without saturation. Open hysteresis loops were found in $M(B)$ measurements only below 15 K. Removing the linear magnetic background shows saturation of the magnetization at $B = 200 - 300$ mT at 5 K, and a coercivity of 60–70 mT. Figure 27 shows the $M(B)$ curves measured between $-500 - 500$ mT for a $Zn_{0.94}Fe_{0.06}O$ sample at 5 and 30 K.

4.2.2 Magnetization measurements on $Zn_{0.99-y}Fe_{0.01}Mg_yO$

Low level of Mg ($y = 0.02$) doping in $Zn_{1-x-y}Fe_xMg_yO$ reduces the magnetization of the samples in comparison with $Zn_{1-x}Fe_xO$ samples having same x. The addition of Mg also introduces a deviation from the Curie–Weiss law at around 50–200 K, where the expected concave shape is replaced by a more linear behaviour. These two phenomena are presented in figure 28, which shows the magnetization of $Zn_{1-x}Fe_xO$ with $x = 0.01$, and $Zn_{1-x-y}Fe_xMg_yO$ with $x = 0.01$ and $y = 0.02$ scaled by the mass of the sample.

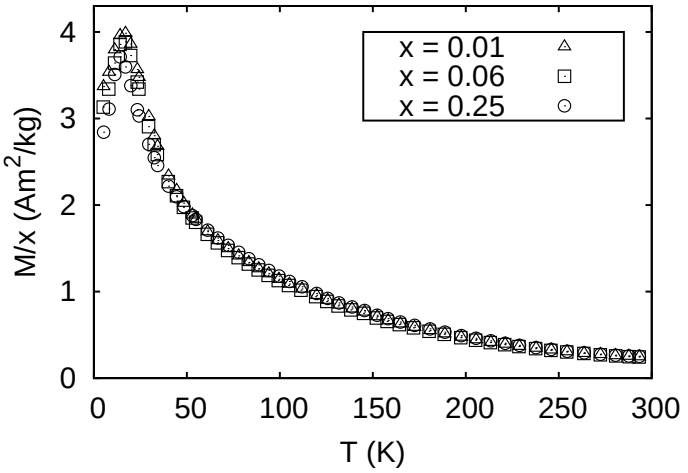

Figure 26. ZFC magnetization curves measured in 100 mT for three $Zn_{1-x}Fe_xO$ samples. The curves are scaled by the Fe content x in the samples. [**P4**]

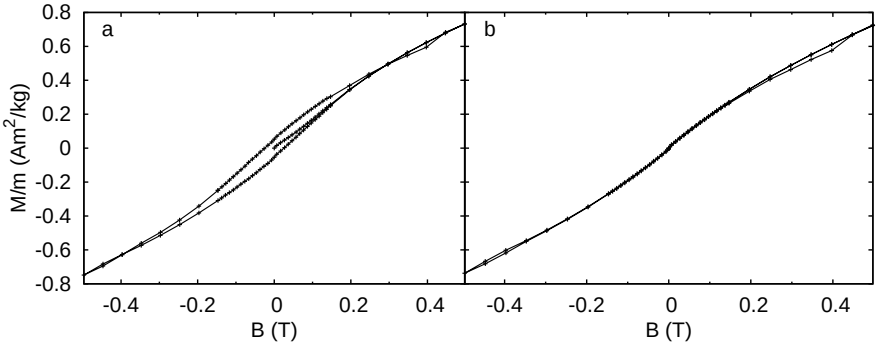

Figure 27. $M(B)$ curves measured for $Zn_{0.94}Fe_{0.06}O$ at 5 K (a) and 30 K (b).

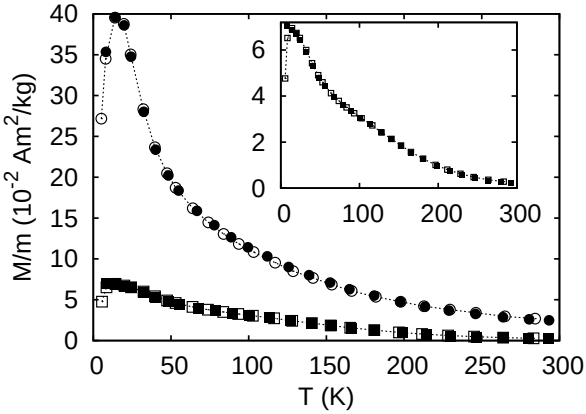

Figure 28. Magnetization curves of $Zn_{0.99}Fe_{0.01}O$ (circles) and $Zn_{0.97}Fe_{0.01}Mg_{0.02}O$ (squares) measured in 100 mT field. Insert: A better view of $Zn_{0.97}Fe_{0.01}Mg_{0.02}O$ magnetization data, where the deviation from Curie–Weiss law can be seen around 50–200 K; the units for the axes are the same as in the larger figure. Open and closed symbols refer to ZFC and FC measurements, respectively. [**P4**]

Increasing the Mg doping while keeping the Fe content low produces convex $M(T)$ curve shapes at $T \gtrsim 45$ K. Compared to $Zn_{0.97}Fe_{0.01}Mg_{0.02}O$ samples, the magnetization is enhanced at the higher measurement temperatures, with the cross-over temperature at $T = 150 - 200$ K. The onset temperature for the rapid increase of the magnetization of $Zn_{0.89}Fe_{0.01}Mg_{0.10}O$ samples is ≈ 320 K.

Figure 29 presents $M(T)$ curves for $Zn_{0.97}Fe_{0.01}Mg_{0.02}O$ and $Zn_{0.89}Fe_{0.01}Mg_{0.10}O$ samples. The increase in low-temperature magnetization of $Zn_{0.89}Fe_{0.01}Mg_{0.10}O$ can be related to single polarons and small clusters of carriers excited thermally from traps in ZnO. Assuming the thermally excited process, the density of the excited carriers, n_c, is given by eq. (23), where n_{c0} is the density of the traps. Fit to the experimental data gives an effective activation energy of 4.3 meV.

Thermoremanent magnetization (TRM) of all these samples reduced rapidly to zero with increasing temperature. A non-zero TRM was measured only below the temperature where ZFC and FC curves separate, *i.e.* below $T \approx 15$ K. The inset in figure 29 presents the measured TRM data for $Zn_{0.97}Fe_{0.01}Mg_{0.02}O$. The magnetization data satisfy the relation (58), which is commonly observed in spin glass type materials [106].

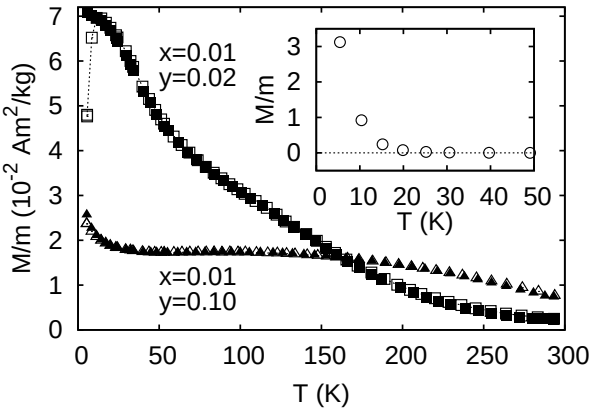

Figure 29. $M(T)$ curves of $Zn_{0.97}Fe_{0.01}Mg_{0.02}O$ and $Zn_{0.89}Fe_{0.01}Mg_{0.10}O$ samples; open and closed symbols refer to ZFC and FC measurements, respectively. Inset: Thermoremanent magnetization of $Zn_{0.97}Fe_{0.01}Mg_{0.02}O$. [**P4**]

4.2.3 Magnetization of $Zn_{0.96-y}Fe_{0.04}Mg_yO$

When the Fe content is increased, the magnetization curves above $T \approx 50$ K for samples with higher Mg content are roughly similar to those observed for $Zn_{0.89}Fe_{0.01}Mg_{0.10}O$. However, the mass magnetization is enhanced by two orders of magnitude by increasing the Fe concentration x from 0.01 to 0.04, and increasing the Mg doping from $y = 0.10$ to $y = 0.26$ at $x = 0.04$ further increases the magnetization. Figure 30 presents the $M(T)$ curves for $Zn_{0.86}Fe_{0.04}Mg_{0.10}O$ and $Zn_{0.7}Fe_{0.04}Mg_{0.26}O$. Derivate of the $M(T)$ data suggests a phase transition with $T_C \approx 330$ K. While MgO was detected as a separate phase in $Zn_{0.7}Fe_{0.04}Mg_{0.26}O$, and MgO is diamagnetic [107, p. E-129], the increase in magnetization with increasing Mg content means that the presence of MgO in the samples does not affect the observed magnetic behaviour.

TRM measurements showed that the $M(T)$ curves of $Zn_{0.86}Fe_{0.04}Mg_{0.10}O$ follow below ≈ 200 K the relation (58). $Zn_{0.7}Fe_{0.04}Mg_{0.26}O$ samples do not satisfy this relation, while the qualitative shapes of TRM and $M_{FC} - M_{ZFC}$ curves are similar. This may be explained by transformation from spin glass to cluster glass type behaviour, where for example anisotropies in the cluster shapes can modify the magnetic properties [87]. The inset in figure 30 presents an example of TRM and $M_{FC} - M_{ZFC}$ curves for a $Zn_{0.7}Fe_{0.04}Mg_{0.26}O$ sample. However, results contradicting the cluster glass behaviour were obtained from TRM measurements at constant temperature as function of measurement time $t_{meas} \leq 4000$ s, when no time dependence was found.

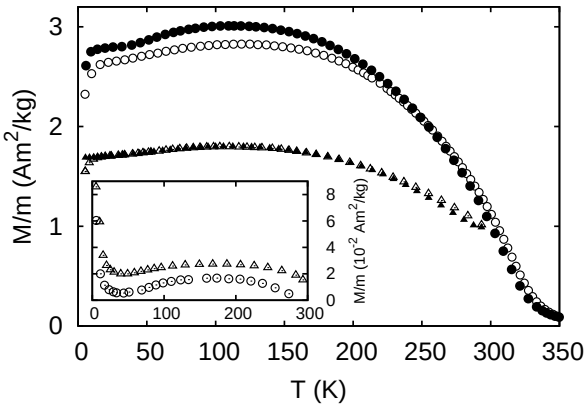

Figure 30. ZFC (open symbols) and FC (closed symbols) magnetizations of $Zn_{0.86}Fe_{0.04}Mg_{0.10}O$ (triangles) and $Zn_{0.7}Fe_{0.04}Mg_{0.26}O$ (circles) samples in 100 mT external field. $Zn_{0.86}Fe_{0.04}Mg_{0.10}O$ data is presented only up to 300 K. Inset: TRM (triangles) and $M_{FC} - M_{ZFC}$ (circles) values for $Zn_{0.7}Fe_{0.04}Mg_{0.26}O$ sample measured in 1 mT field. [**P4**]

$M(B)$ data for $Zn_{0.7}Fe_{0.04}Mg_{0.26}O$ shows saturation of the magnetization in 100–200 mT fields. No open hysteresis loops were found between 5 and 300 K, contrary to expectations from the cluster glass model. $M(B)$ curves measured at 100 and 300 K are shown in figure 31. The complex magnetic behaviour of $Zn_{0.7}Fe_{0.04}Mg_{0.26}O$, and to a lesser degree in $Zn_{0.86}Fe_{0.04}Mg_{0.10}O$, could not be described by any simple model of magnetic interactions in the sample. While the data partially supports a model of weakly correlated ferromagnetic clusters, the observed behaviour is similar to ”phantom ferromagnetism” in some other doped DMS materials [108].

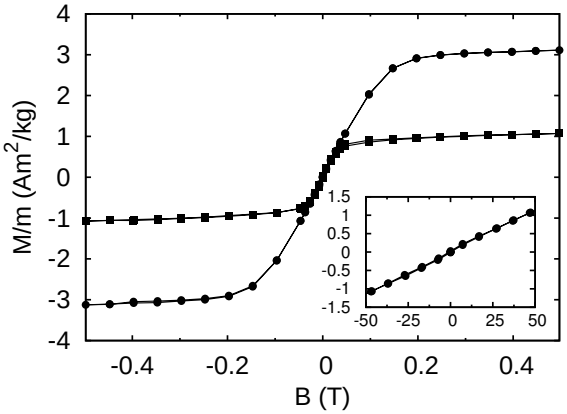

Figure 31. $M(B)$ curves of $Zn_{0.7}Fe_{0.04}Mg_{0.26}O$ sample measured at 100 (circles) and 300 K (squares). Inset: Magnification of the 100 K data with -50 mT $\leq B \leq 50$ mT. [**P4**]

4.2.4 Thermally activated RKKY interaction in $Zn_{1-x-y}Fe_xMg_yO$

Simulations of thermally activated RKKY interaction presented in chapter 1.3.2 were made with eqs. (28) and (23), which were solved numerically for each point at a constant temperature, using electron spin $s = \frac{1}{2}$, Fe^{3+} spin $S = \frac{5}{2}$, and the lattice constant $a =$ 0.325 nm. The temperature range was 20–350 K in the simulations, and the $\frac{\langle S_z \rangle}{S}$ values were solved at 1 K intervals.

Parameters n_{c0}, Δ, n_i, and J were varied to obtain different simulated curve shapes. Comparing the simulations with experimental $Zn_{0.96-y}Fe_{0.04}Mg_yO$ with $y = 0.10$ or 0.26 magnetization data showed qualitatively similar curve shapes at $100 \lesssim T \lesssim 330$ K with parameter values $n_{c0} \sim 3.5 \cdot 10^{20}$ cm^{-3}, $\Delta \sim 10$ meV, $n_i \sim 4 \cdot 10^{21}$ cm^{-3}, and $J \sim$ 1 eV. Figure 32 presents an example of the simulations with $\Delta = 12$ meV, $J = 1.1$ eV, $n_{c0} = 3.5 \cdot 10^{20}$ cm^{-3}, and $n_i = 4 \cdot 10^{21}$ cm^{-3}, and a comparison to measured data for $Zn_{0.7}Fe_{0.04}Mg_{0.26}O$.

Comparisons with measured parameters for ZnO samples show that the simulations are reasonably close to their expected values. For $Zn_{0.7}Fe_{0.04}Mg_{0.26}O$, the calculated value of n_i samples is $\sim 2 \cdot 10^{21}$ cm^{-3}, a factor of two lower than the value in the simulations. n_{c0} values are in a realistic range, as carrier concentrations well above 10^{21} cm^{-3} have been reported [109] for doped ZnO samples.

The explanation for the simulations deviating from the experimental data is twofold: At low temperatures, when the carrier concentration is diminishing, other processes that

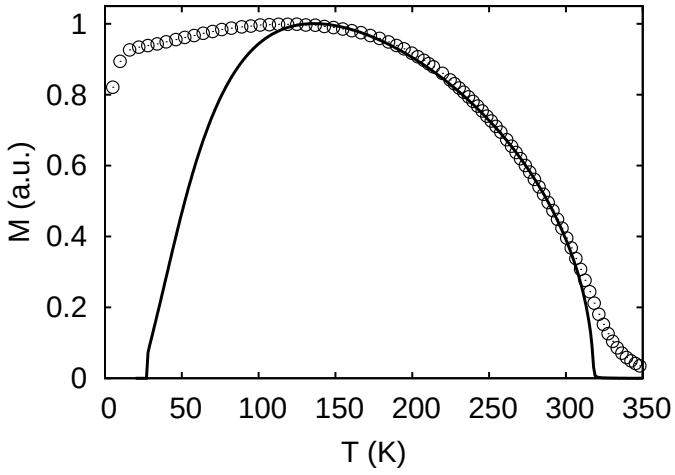

Figure 32. The result of simulation of thermally activated RKKY interaction from eq. (28) with $\Delta = 12$ meV, $J = 1.1$ eV, $n_{c0} = 3.5 \cdot 10^{20}$ cm^{-3}, and $n_i = 4 \cdot 10^{21}$ cm^{-3} (line), and the ZFC magnetization data of $Zn_{0.7}Fe_{0.04}Mg_{0.26}O$ (points). Both the numerical simulation and the measured magnetization data are scaled to $M_{\max} = 1$. [**P4**]

do not depend on free charge carriers may dominate the magnetic behaviour [62]. An example of such a process is polaron percolation, as presented in chapter 1.3.3. On the other hand, approaching T_C from above, the critical behaviour of ferromagnets [110, pp. 80–81] may explain the divergence between the simulations and experimental data at high temperatures, as the simulation does not take the critical behaviour into account.

4.2.5 Critical behaviour of $Zn_{1-x-y}Fe_xMg_yO$ above T_C

Percolation model of ferromagnetism [77, pp. 94–136] starts with assumption of small, weakly correlated ferromagnetic clusters above T_C. The size and correlation length λ of these clusters grows with lowering temperature. A critical behaviour sets in when the correlation length exceeds much the lattice parameter of the material. The dependence of λ on mean distance between the clusters, R, is given [111] as

$$\lambda \approx R \left(\frac{T}{T_C} - 1 \right)^{-\nu}, \tag{76}$$

where

$$R \approx 2 \left(\frac{4\pi N}{3} \right)^{-\frac{1}{3}} \left(\frac{T}{T_C} - 1 \right)^{-\nu}, \tag{77}$$

and $\nu \approx 1$ is the critical exponent for the correlation length. The volume fraction of the ferromagnetic cluster, η, satisfies the equation [111]

$$\eta = 1 - e^{-\frac{4\pi N r^3}{3}}, \tag{78}$$

where N is the density of the clusters, and r is the cluster radius. The critical value for the volume fraction, η_{cr}, is [77, p. 117]

$$\eta_{cr} = 0.29. \tag{79}$$

Treating the ferromagnetic clusters as a system of uncorrelated magnetic moments, the magnetization at the critical temperature T_{cr} ($\eta(T_{cr}) = 0.29$) is roughly

$$M(T_{cr}) \approx \mu N \mathscr{L}\left(\frac{\mu B}{k_{\mathrm{B}} T_{cr}}\right), \tag{80}$$

where $\mathscr{L}(x)$ is the Langevin function. For $x \ll 1$, $\mathscr{L}(x) \approx \frac{1}{3}x$, and the magnetization is

$$M(T_{cr}) \approx \frac{\mu^2 N}{3 k_{\mathrm{B}} T_{cr}}. \tag{81}$$

Approximating the volume fraction with

$$\eta \approx \frac{\mu N}{M_s}, \tag{82}$$

where M_s is the saturation magnetization, we get

$$\mu \approx \frac{3 k_{\mathrm{B}} T_{cr} \chi(T_{cr})}{M_s \eta} \tag{83}$$

and

$$N \approx \frac{\eta^2 M_s^2}{3 k_{\mathrm{B}} T_{cr} \chi(T_{cr})}, \tag{84}$$

where $\chi(T_{cr})$ is the magnetic susceptibility.

The measured magnetization data for $Zn_{0.7}Fe_{0.04}Mg_{0.26}O$ gives $M_s \approx 1960\ \frac{\mathrm{A}}{\mathrm{m}}$, $T_{cr} \approx 330$ K, and $\chi(T_{cr}) \approx 12.8 \cdot 10^3\ \frac{\mathrm{J}}{\mathrm{T^2 m^3}}$. Using these values in eqs. (78), (83), and (84), we get [**P4**] the following estimates: The cluster radius $r \approx 40$ nm, the cluster concentration $N \approx 1.1 \cdot 10^{21}\ \frac{1}{\mathrm{m^3}}$, and the cluster magnetization $\mu \approx 43 \cdot 10^3\ \mu_{\mathrm{B}}$.

An analysis of the critical exponents γ at temperatures above T_{C} can be done by writing the scaling law near T_{C} in the form [111]

$$\chi^{-1} - \chi_{\mathrm{C}}^{-1} \sim \left(\frac{T}{T_{\mathrm{C}}} - 1\right)^{\gamma}, \tag{85}$$

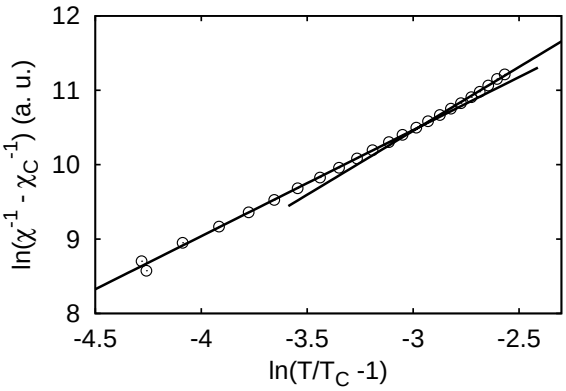

Figure 33. Critical behaviour of the magnetic susceptibility of $Zn_{0.7}Fe_{0.04}Mg_{0.26}O$ above T_C [**P4**].

where $\chi_C = \chi(T_C)$. Eq. (85) can be used to find γ from linear fits to plots of $\ln(\chi^{-1} - \chi_C^{-1})$ vs. $\ln\left(\frac{T}{T_C} - 1\right)$. Figure 33 shows these plots and fits for a $Zn_{0.7}Fe_{0.04}Mg_{0.26}O$ sample. A change in the critical exponent γ can be observed, with the obtained γ values $\gamma_1 = 1.43 \pm 0.03$ and $\gamma_2 = 1.75 \pm 0.04$, corresponding to 3D Heisenberg model [110] and 3D cluster percolation [112], respectively.

4.3 Magnetic resonance experiments

Electron paramagnetic resonance spectra of Fe^{3+} of $Zn_{1-x}Fe_xO$ samples at 4.2 K show reduction in intensity with growing x. The spectra for $x = 0.01$ and 0.066 are presented in figure 34(a). A likely explanation for the change in the intensity is an increase in the interactions between the Fe^{3+} ions. The spectra can be described with a spin Hamiltonian [113, 114], using Fe^{3+} spin $S = \frac{5}{2}$, an isotropic g-factor $g = 2.006$ [115], and anisotropic crystal field fine structure parameters $D = -593.7 \cdot 10^{-4}$ cm^{-1}, $F = 4 \cdot 10^{-4}$ cm^{-1}, and $a = 39 \cdot 10^{-4}$ cm^{-1}. An example of the EPR spectra simulations is presented in figure 34(b).

A resonance line observed at room temperature around 330 mT in the EPR spectra of $Zn_{1-x}Fe_xO$ samples splits with lowering temperature to two lines, ”A” and ”B”. The position of the A line is shifted nearly linearly towards lower magnetic fields when the temperature is lowered. At T below ≈ 35 K, both lines shift rapidly to lower fields, while the ”B” line resonance field is nearly constant above 50 K. Figure 35(a) shows the splitting of the resonance line, and the line positions are plotted in figure 36.

Mg co-doping modifies the EPR spectra, as presented in figure 34(b). The ”A” and ”B” lines observed in the magnetic resonance signals of are replaced by another line close to the position of the ”B” line. The temperature dependence of the position of this ”C” line is similar to the ”B” line, without the rapid decrease at the low temperatures. The ”C” line positions are presented in figures 35(b) and 36.

The similarities in the temperature dependences of ”B” and ”C” line positions suggest that they are connected to $Fe^{3+}-Fe^{3+}$ pairs [116]. The line shifts can be explained by increasing Weiss field caused by ordering of the magnetic moments in the samples [117]. As the ”A” line was not detected in samples with Mg content $y \geq 0.10$, it can be attributed to Fe^{3+} ions in the impurity phase.

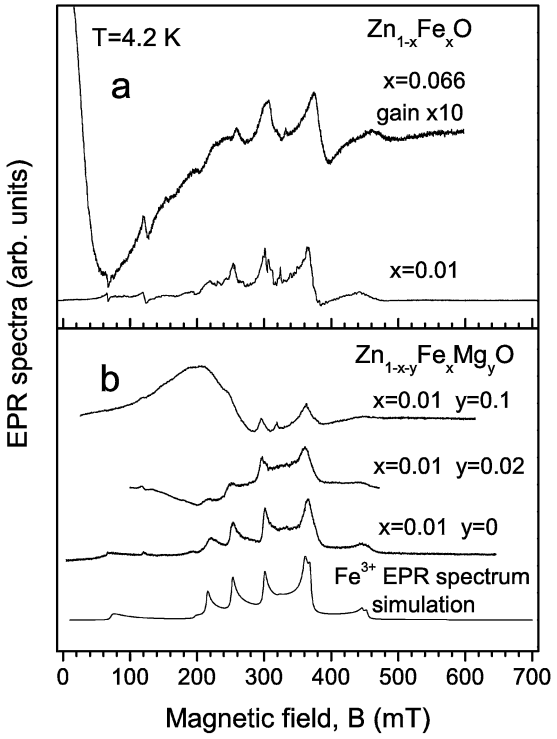

Figure 34. Fe^{3+} EPR spectra measured for $Zn_{1-x}Fe_xO$ (a) and $Zn_{1-x-y}Fe_xMg_yO$ (b) samples at 4.2 K. EPR spectrum simulation is included. [**P4**]

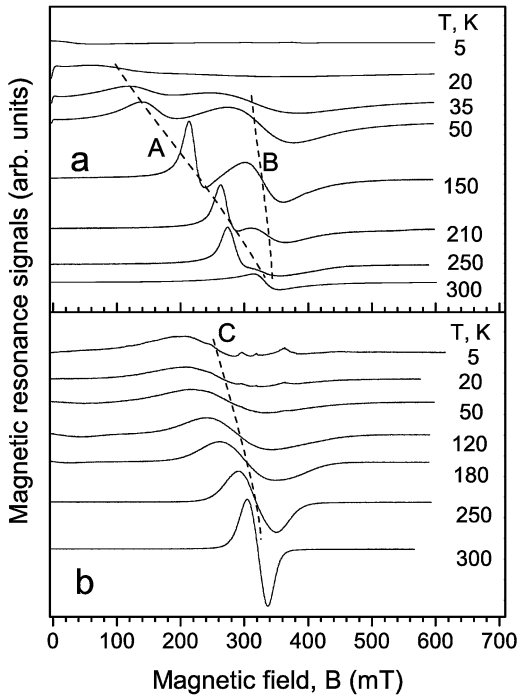

Figure 35. (a) EPR lines in $Zn_{0.94}Fe_{0.06}O$. With lowering the temperature, the resonance line splits to two lines, marked ”A” and ”B”. (b) Resonance line ”C” is observed in $Zn_{0.89}Fe_{0.01}Mg_{0.10}O$. [**P4**]

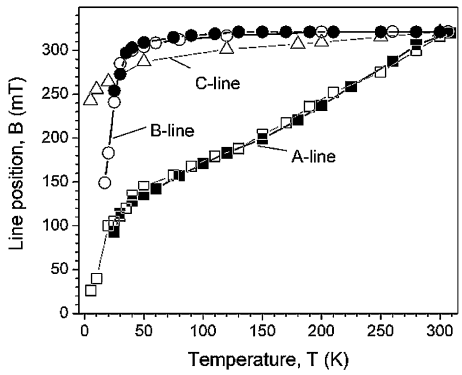

Figure 36. Positions of ”A” and ”B” lines in $Zn_{0.99}Fe_{0.01}O$ (closed symbols) and $Zn_{0.94}Fe_{0.06}O$ (open symbols), and ”C” line in $Zn_{0.89}Fe_{0.01}Mg_{0.10}O$ (triangles). [**P4**]

4.4 Discussion

Based on XRD, EPR, and magnetic measurements data, it is clear that magnetic properties of $Zn_{1-x}Fe_xO$ are dominated by impurities in the samples. No difference was found between the samples prepared by two different chemical reactions, and the same impurity phase has been observed in the samples prepared by several other methods [118–120]. While the XRD data does not allow differentiation between Fe_3O_4 and $ZnFe_2O_4$, the magnetic behaviour strongly points towards the latter. Cation disorder enhancing ferromagnetic interactions above 10 K may explain the increased magnetic transition temperature of $ZnFe_2O_4$ [118].

Chemical phase separation of the samples means that we cannot use theoretical predictions [19, 40] of T_C for $Zn_{1-x}Fe_xO$ materials. Additionally, a wide variety of magnetic behaviours have been reported for magnetic oxide materials (for discussion, see [15]). As the observed behaviour depends on the chemical method used for sample preparation [108, 119], and on other factors in the sample preparation process like reaction temperature [120], our results suggest that in many cases the magnetism of ZnO doped with transition metals is dominated by separate chemical phases, or local areas with higher than average transition metal (TM) ion concentrations.

Charge-transfer ferromagnetism has been proposed [108] as the model of magnetic interactions for the ferromagnetic $Zn_{1-x}TM_xO$ nanoparticle samples [121, 122]. In this model, electron density on the particle surfaces is enhanced by charge transfer from bulk of the particle to defect states at the surface. Consequently, Fermi level of the local electron density of states in the surface layer raises leading to a state where the Stoner criterion is satisfied.

Magnetization of $Zn_{0.97}Fe_{0.01}Mg_{0.02}O$ can also be attributed mainly to the $ZnFe_2O_4$ phase. The reduction in the magnetization compared to the samples without Mg co-doping means that fewer Fe ions enter the impurity phase. The deviation from Curie–Weiss law gives evidence of secondary magnetic interactions, similar to those observed in the samples with higher Mg content.

RKKY interaction combined with thermal excitation of the carriers and carrier-mediated ferromagnetism [67] provides an explanation for the magnetic properties of $Zn_{1-x-y}Fe_xMg_yO$ with $y \geq 0.10$, above ≈ 100 K. Co-doping with Mg provides more free carriers, and as they interact with the magnetic impurities, there is a ferromagnetic coupling between the Fe ions. This mechanism also explains the dramatic increase of the magnetization of $Zn_{0.96-y}Fe_{0.04}Mg_yO$ compared to $Zn_{0.99-y}Fe_{0.01}Mg_yO$, as the RKKY interaction strongly depends on the average distance between the magnetic ions.

The magnetic properties of $Zn_{1-x-y}Fe_xMg_yO$ with $x \geq 0.04$ and $y \geq 0.10$ suggest that it can be considered as a viable material for spintronics applications. However, utilizing $Zn_{1-x-y}Fe_xMg_yO$ as a magnetic layer in MRAM may be difficult, as no hysteresis was observed in the bulk material. The next step towards practical applications is the manufacture and characterization of $Zn_{1-x-y}Fe_xMg_yO$ thin films. Optimization of the Fe and Mg doping levels is required, and a third dopant element might be needed to further improve the magnetic properties. If those properties prove useful, existing technologies can be used to integrate ZnO-based materials into electronics components relatively easily [36].

5 Conclusions

In this thesis, I have investigated two different semiconductor materials doped with transition metal ions. The first material, CdSb doped with 2 atomic percent of Ni, shows anisotropic electric and magnetic properties in regard to the different crystallographic directions. Magnetic irreversibility is observed in low fields below 300 K, but the irreversibility is suppressed in increasing fields, disappearing above the anisotropy field $B_{\mathrm{K}} \sim 400$ mT. Similar behaviour is observed for the blocking temperature in ZFC magnetization data, where the magnetization has a broad maximum around T_b.

Saturation of the magnetization is observed in external fields of $2-3$ T, while the magnetic field dependence of the magnetization only weakly depends on the measurement temperature at 100–300 K. Below 100 K, the saturation magnetization is enhanced, which can be attributed to the paramagnetic contribution of single Ni ions and small ion clusters in the sample. Coercivity shows a crossover from weak to strong dependence on the temperature when temperature is lowered below T_b. The anisotropy of the coercivity is inverted in regard to the crystal axes compared to the anisotropy of the saturation magnetization.

We conclude that the magnetic properties of Ni-doped CdSb are dominated by spheroidal nanoparticles consisting of $\mathrm{Ni}_{1-x}\mathrm{Sb}_x$, where $x \leq 0.038$. These particles are oriented around a preferred direction, and have a high aspect ratio and wide size distribution. Indications of two different magnetization reversal modes for the nanoparticles are observed. While anisotropies of the saturation magnetizations and the coercivities combined with the observed relation $B_c \ll B_{\mathrm{K}}$ suggest magnetization reversal by curling, the magnetic field dependences of the blocking temperatures are more typical for reversal by rotation. This discrepancy can be explained by wide cluster size distribution, with the average cluster size in the cross-over region between the two reversal modes.

Variable-range hopping (VRH) behaviour is observed in low-temperature conductivity of the CdSb samples in zero external magnetic field. The resistance data suggests two types of hopping mechanisms: Shklovskii–Efros VRH along [100] and [001] crystallographic axes, and Mott VRH in [010] direction. In non-zero external magnetic field below the weak field limit, where the resistivity ρ follows the law $\rho \sim B^2$, the hopping mechanisms are nearest-neighbour hopping in [010] and [001] directions, whereas [100] direction shows the Mott VRH. The weak field type dependence of the resistivity on external magnetic field was observed below $B \sim 6$ T. The difference between the hopping mechanisms in zero external field and in the weak field regime can be attributed to intrinsic magnetic disorder in Ni-doped CdSb samples.

The second material under investigation was ZnO doped with Fe and Mg. The ZFC and FC magnetizations of all the $Zn_{1-x}Fe_xO$ samples are qualitatively similar, and strictly proportional to the Fe content in the samples. The ZFC and FC magnetizations have a maximum at ~ 15 K, and both follow Curie–Weiss law at higher temperatures. This maximum is attributed to a secondary chemical phase observed in the XRD measurements. The best candidate for this impurity phase is $ZnFe_2O_4$.

Low levels of Mg co-doping reduce the mass magnetization and cause a deviation from Curie–Weiss law at 50–200 K. Increasing the Mg concentration while keeping the Fe content low, the ZFC and FC magnetization curves transform from a concave to a convex shape, with a weak temperature dependence between 50 and 200 K, and a more rapid increase below ~ 45 K. As the XRD measurements show that the secondary chemical phase disappears with increasing Mg content, it is clear that the presence of Mg in the samples increases the solubility of Fe into the ZnO host lattice. The magnetic properties of $Zn_{0.97}Fe_{0.01}Mg_{0.02}O$ are thus explained by two competing magnetic phases in the sample, as some Fe is still available for forming the $ZnFe_2O_4$ phase.

$Zn_{1-x-y}Fe_xMg_yO$ samples with $x = 0.04$ and $y \geq 0.10$ show an increase in the mass magnetization by two orders of magnitude compared to $x = 0.01$ samples. The shapes of the ZFC and FC magnetization curves suggest ferromagnetic type magnetization, with T_C around 320–330 K. Magnetic irreversibility is observed in ZFC and FC measurements of $Zn_{0.7}Fe_{0.04}Mg_{0.26}O$, but contradictingly, the $M(B)$ curves do not exhibit open loops. A thermally activated RKKY mechanism is proposed to explain the high-temperature magnetization of these samples, supported by computer simulations based on theoretical model. In this model, the large difference in magnetization between $x = 0.01$ and 0.04 samples rises from decreased average distance between the magnetic ions, leading to stronger ferromagnetic coupling. A secondary process such as polaron percolation is required in the low-temperature regime.

References

[1] M. N. Baibich, J. M. Broto, and A. Fert, Phys. Rev. Lett. **61**, 2472 (1988).

[2] S. A. Wolf *et al.*, Science **294**, 1488 (2001).

[3] S. Tehrani *et al.*, IEEE Trans. Magn. **35**, 2814 (1999).

[4] S. S. P. Parkin *et al.*, J. Appl. Phys. **85**, 5828 (1999).

[5] B. N. Engel *et al.*, IEEE Trans. Magn. **41**, 132 (2005).

[6] S. Tehrani *et al.*, Proc. IEEE **91**, 703 (2003).

[7] J.-G. Zhu, Proc. IEEE **96**, 1786 (2008).

[8] W.H. Butler and A. Gupta, Nat. Mater. **3**, 845 (2004).

[9] G. Prenat *et al.*, IEEE Trans. Magn. **45**, 3400 (2009).

[10] W.H. Kautz, IEEE Trans. Comput. **18**, 719 (1969).

[11] S. Matsunaga *et al.*, Appl. Phys. Expr. **1**, 091301 (2008).

[12] S. Das Sarma, American Scientist **89**, 516 (2001).

[13] Y.B. Xu *et al.*, J. Magn. and Magn. Mater. **304**, 69 (2006).

[14] A. Bonanni and T. Dietl, Chem. Soc. Rev. **39**, 528 (2010).

[15] J. M. D. Coey, Current Opinion in Solid State and Materials Science **10**, 83 (2006).

[16] J. M. D. Coey, M. Venkatesan, and C. B. Fitzgerald, Nature Materials **4**, 173 (2005).

[17] S.J. Pearton *et al.*, J. Appl. Phys. **93**, 1 (2003).

[18] H. Ohno, J. Magn. and Magn. Mater. **200**, 110 (1999).

[19] T. Dietl *et al.*, Science **287**, 1019 (2000).

[20] G. T. Thaler *et al.*, Appl. Phys. Lett. **80**, 3964 (2002).

[21] P. Sharma *et al.*, Nature Mater. **2**, 673 (2003).

[22] R. M. Frazier *et al.*, J. Appl. Phys. **94**, 1592 (2003).

[23] F. J. Owens, J. Phys. Chem. Solids **66**, 793 (2005).

[24] T. Fukumura *et al.*, Appl. Surf. Sci. **223**, 62 (2004).

[25] E. K. Arushanov, Prog. Crystal Growth and Charact. **13**, 1 (1986).

[26] K. A. Almin, Acta Chem. Scand. **2**, 400 (1948).

[27] R. Laiho *et al.*, J. Phys. Cond. Mat. **16**, 333 (2004).

[28] M. Matyáš, Czech J. Phys. **B17**, 227 (1967).

[29] S.F. Marenkin, M. Saidullaeva, V.P. Sanygin, and I.S. Kovaleva, Izv. Akad. Nauk SSSR, Neorg. Mater. **18**, 1759 (1982).

[30] A. Müller and M. Wilhelm, J. Phys. Chem. Solids **26**, 2021 (1965).

[31] E. Kneller, *Ferromagnetismus* (Springer-Verlag, 1962).

[32] Y. Chen *et al.*, J. Appl. Phys. **84**, 3912 (1998).

[33] S. J. Pearton *et al.*, Progress in Materials Science **50**, 293 (2005).

[34] C. Agashe *et al.*, Thin Solid Films **442**, 167 (2002).

[35] H. Kim *et al.*, Appl. Phys. Lett. **90**, 203508 (2007).

[36] F. Pan *et al.*, Materials Science and Engineering R **62**, 1 (2008).

[37] A. Y. Polyakov *et al.*, J. Vac. Sci. Technol. B **23**, 274 (2005).

[38] N. H. Hong *et al.*, Phys. Rev. B **72**, 045336 (2005).

[39] X. X. Wei *et al.*, J. Phys. Cond. Mat. **18**, 7471 (2006).

[40] L. M. Sandratskii and P. Bruno, Phys. Rev. B **73**, 045203 (2006).

[41] H. Pan *et al.*, Phys. Rev. Lett. **99**, 127201 (2007).

[42] X. G. Xu *et al.*, Appl. Phys. Lett. **97**, 232502 (2010).

[43] D. Sanyal *et al.*, J. Phys. Cond. Mat. **20**, 045217 (2008).

[44] M. Khalid *et al.*, Phys. Rev. B **80**, 035331 (2009).

[45] X. Zuo *et al.*, J. Appl. Phys. **105**, 07C508 (2009).

[46] C. Peng *et al.*, J. Phys. Chem. C **116**, 9709 (2012).

[47] C. P. Bean and J. D. Livingston, J. Appl. Phys. **30**, S120 (1959).

[48] L. Neél, Ann. Geophys. **5**, 99 (1949).

[49] E.P. Wohlfarth, J. Phys. F: Metal Phys **10**, L241 (1980).

[50] E. H. Frei, S. Shtrikman, and D. Treves, Physical Review **106**, 446 (1957).

[51] L. Sun, Y. Hao, C.-L. Chien, and P.C. Searson, IBM J. Res. and Dev. **49**, 79 (2005).

[52] B. D. Cullity, *Introduction to Magnetic Materials* (Addison-Wesley Publishing Company, Inc., 1972).

[53] A. Aharoni, J. Appl. Phys. **82**, 1281 (1997).

[54] H. Q. Yin and W. D. Doyle, J. Appl. Phys. **91**, 7709 (2002).

[55] R. M. Bozorth, *Ferromagnetism* (D. Van Norstrand Company, Inc., 1959).

[56] P. Gaunt, Phil. Mag. B **48**, 261 (1983).

[57] C. Zener, Physical Review **81**, 440 (1951).

[58] T. Kasuya, Progr. Theoret. Phys. **16**, 45 (1956).

[59] M.A. Ruderman and C. Kittel, Phys. Rev. **96**, 99 (1954).

[60] J. H. Van Vleck, Reviews of Modern Physics **34**, 681 (1962).

[61] K. Yosida, Phys. Rev. **106**, 893 (1957).

[62] M.J. Calderón and S. Das Sarma, Phys. Rev. B **75**, 235203 (2007).

[63] E.A. Pashitskii and S.M. Ryabchenko, Sov. Phys. Solid State **79**, 322 (1979).

[64] M. Berciu and R. N. Bhatt, Phys. Rev. B **69**, 045202 (2004).

[65] J. Crangle, *Solid State Magnetism* (Edward Arnold, A division of Hodder & Stoughton, LONDON MELBOURNE AUCKLAND, 1991).

[66] T. Dietl and J. Spałek, Phys. Rev. B **28**, 1548 (1983).

[67] M. J. Calderón and S. Das Sarma, Annals of Physics **322**, 2618 (2007).

[68] S. Das Sarma, E. H. Hwang, and A. Kaminski, Phys. Rev. B **67**, 155201 (2003).

[69] A. F. Kohan, G. Ceder, D. Morgan, and C. G. Van de Walle, Phys. Rev. B **61**, 15019 (2000).

[70] H.-J. Lee, S.-Y. Jeong, C. R. Cho, and C. H. Park, Appl. Phys. Lett. **81**, 4020 (2002).

[71] W. Pauli, Z. Phys. **41**, 81 (1927).

[72] J.B. Goodenough, *Magnetism and the Chemical Bond* (John Wiley & Sons, 1966).

[73] F. Brailsford, *Physical Principles of Magnetism* (D. Van Nostrand Company LTD., 1966).

[74] K.H.J. Buschow, *Magnetic and superconducting materials* (Amanda Weaver, 2005).

[75] N. F. Mott, Phil. Mag. **19**, 835 (1969).

[76] R. Laiho *et al.*, J. Phys. Cond. Mat. **14**, 8043 (2002).

[77] B. I. Shklovskii and A. L. Efros, *Electronic Properties of Doped Semiconductors* (Springer-Verlag Berlin Heidelberg, 1984).

[78] M. Pollak, Discuss. Faraday Soc. **50**, 13 (1970).

[79] V. Ambegaokar, B. I. Halperin, and J. S. Langer, Phys. Rev. B **4**, 2612 (1971).

[80] A. L. Efros and B. I. Shklovskii, J. Phys. C: Solid State Phus. **8**, L49 (1975).

[81] W. Martienssen and H. Warlimont, *Springer Handbook of Condensed Matter and Materials Data* (Springer, 2005).

[82] M. Viret, L. Ranno, and J. M. D. Coey, Phys. Rev. B **55**, 8067 (1997).

[83] L. Essaleh *et al.*, Phys. Rev. B **52**, 7798 (1995).

[84] R. Laiho *et al.*, J. Phys. Cond. Mat. **20**, 295204 (2008).

[85] E. Blinov *et al.*, Supercond. Sci. Technol. **10**, 818 (1997).

[86] B. Lax and K. J. Button, *Microwave ferrites and ferrimagnetics* (McGraw-Hill Book Company, Inc., 1962).

[87] N. A. Belous *et al.*, Sov. Phys. Solid State **35**, 887 (1990).

[88] S. Zhou *et al.*, Phys. Rev. B **80**, 174423 (2009).

[89] D. Pajić *et al.*, J. Phys. Cond. Mat. **19**, 296207 (2007).

[90] A. R. de Moraes *et al.*, J. Appl. Phys. **103**, 123714 (2008).

[91] N. W. Ashcroft and N. D. Mermin, *Solid State Physics* (W. B. Sounders Company, 1976), ssp.

[92] J. I. MacNab and R. B. Anderson, J. Catal. **29**, 328 (1973).

[93] R. Laiho, K. G. Lisunov, E. Lähderanta, and V. S. Zakhvalinskii, J. Phys. Cond. Mat. **11**, 555 (1999).

[94] L. Essaleh *et al.*, Phys. Rev. B **50**, 18040 (1994).

[95] A. N. Ionov, I. S. Shimak, and M. N. Matveev, Solid State Commun. **47**, 763 (1984).

[96] E. Arushanov *et al.*, J. Appl. Phys. **100**, 113704 (2006).

[97] A. L. Efros, B. Skinner, and B. I. Shklovskii, Phys. Rev. B **84**, 064204 (2011).

[98] K. M. Itoh *et al.*, J. Phys. Soc. Jpn. **73**, 173 (2004).

[99] J. Raittila, H. Huhtinen, P. Paturi, and Yu. P. Stepanov, Physica C **371**, 90 (2002).

[100] C. Yao *et al.*, J. Phys. Chem. C **111**, 12274 (2007).

[101] W. B. Mi *et al.*, J. Phys. D: Appl. Phys. **41**, 055009 (2008).

[102] M. E. Straumanis and L. S. Yu, Acta Cryst. **A25**, 676 (1969).

[103] F. C. Wellstood, J. J. Kingston, and John Clarke, J. Appl. Phys. **75**, 683 (1994).

[104] S. Raghavan, J.P. Hajra, G.N.K. Iyengar, and K.P. Abraham, Thermochimica Acta **189**, 151 (1991).

[105] S. A. Oliver, H. H. Hamdeh, and J. C. Ho, Phys. Rev. B **60**, 3400 (1999).

[106] V. Tsurkan, M. Baran, R. Szymczak, and H. Szymczak, J. Magn. and Magn. Mater. **172**, 317 (1997).

[107] R. C. Weast (ed.), *Handbook of Chemistry and Physics* (The Chemical Rubber Co., 1970-1971).

[108] J. M. D. Coey, K. Wongsaprom, J. Alaria, and M. Venkatesan, J. Phys. D: Appl. Phys. **41**, 134012 (2008).

[109] J. G. Lu *et al.*, J. Appl. Phys. **101**, 083705 (2007).

[110] M. E. Fisher, *Proceedings of the International Conference on Magnetism* (The Institute of Physics and the Physical Society, Nottingham, 1964).

[111] R. Laiho *et al.*, J. Magn. and Magn. Mater. **293**, 892 (2005).

[112] S. Kirkpatrick, Phys. Rev. Lett. **36**, 69 (1976).

[113] S. Geschwind, Phys. Rev. **121**, 363 (1961).

[114] X. Y. Kuang, Phys. Stat. Sol. (b) **197**, 225 (1996).

[115] Jr. W. M. Walsh and Jr. L. W. Rupp, Phys. Rev. **126**, 952 (1962).

[116] R. Bramley and M. B. McCool, J. Phys. C: Solid State Phys. **9**, 1793 (1976).

[117] T. S. Altshuler, Yu. V. Goryunov, and A. V. Nateprov, JPCS **324**, 012020 (2011).

[118] M.D. Carvalho, L.P. Ferreira, R.P. Borges, and M. Godinho, J. Solid State Chem. **185**, 160 (2012).

[119] V. K. Sharma and G. D. Varma, Adv. Mat. Lett. **3**, 126 (2012).

[120] O. D. Jayakumar, I. K. Gopalakrishnan, and S. K. Kulshreshtha, J. Mater. Sci. **41**, 4706 (2006).

[121] X. Wang *et al.*, Appl. Phys. Lett. **88**, 223108 (2006).

[122] J. Alaria, M. Venkatesan, and J. M. D. Coey, J. Appl. Phys. **103**, 07D123 (2008).